# Online beam phase and current calibration for rf cavities under closed-loop operation

Feng Qiu,[1,2,*] Rihua Zeng,[3] Chengye Xu,[1] Shihui Wei,[1] Lijuan Yang,[1] Zhaojie Chen,[1,2] Yilin Miao,[1,2] Muyuan Wang,[4] Cecilia Maiano,[4] Paolo Pierini,[4] and Yuan He[1,2,†]

[1]*Institute of Modern Physics, Chinese Academy of Sciences, Lanzhou, 730000, China*
[2]*School of Nuclear Science and Technology, University of Chinese Academy of Sciences, Beijing 100049, China*
[3]*Advanced Energy Science and Technology Guangdong Laboratory, Huizhou, 516000, China*
[4]*European Spallation Source, ERIC, 22100, Lund, Sweden*

(Received 18 November 2025; accepted 21 May 2026; published 29 June 2026)

Leveraging the interaction between the beam and the radio-frequency (rf) cavity to measure the beam phase reduces tuning time and mitigates slow drifts induced by ambient conditions. An online phase-measurement approach based on beam-induced rf transients was previously demonstrated at DESY using superconducting rf cavities in an electron accelerator under open-loop operation. However, open-loop operation is unsuitable for high-current proton or heavy-ion linacs due to elevated risks of beam loss and trips. This work proposes two novel schemes that operate under closed-loop conditions. The first, a virtual open-loop (VOL) method, solves the cavity difference equation to remove the contribution of feedback (and/or feedforward) control from the cavity field, thereby recovering the beam-loading signal under an equivalent open-loop condition from which the beam parameters are determined. The second, a steady-state (SS) method, determines the beam parameters (i.e., beam current and phase) when beam-loading and cavity-detuning compensation are sufficient and infers the beam phase and current by computing the vector difference of steady-state forward voltages with and without beam. Both approaches were systematically validated on the buncher cavity at the European Spallation Source (ESS), showing agreement with independent beam diagnostics, with phase error within $\pm 0.5°$ and current error within $\pm 4\%$. The methods enable real-time, accurate beam-phase measurement during closed-loop operation and are readily extensible to other high-power accelerator systems.

DOI: 10.1103/jrx8-jhrm

## I. INTRODUCTION

Located in Lund, Sweden, the European Spallation Source (ESS) is a high-intensity proton linear accelerator under construction. As is shown in Table I, it is designed for 5 MW operation with a final beam energy of 2 GeV [1]. The linac comprises a normal-conducting (NC) front end at 352.21 MHz followed by a superconducting (SC) section at 704.42 MHz, excluding the spoke cavities. Figure 1 shows the Drift Tube Linac (DTL) and SC sections divided into tanks and cryomodules; gray modules will be unpowered during the initial 800 MeV, 2 MW phase [2–4]. Achieving the nominal 62.5 mA peak beam current at 14 Hz requires tight rf phase control in each cavity to preserve beam quality and limit losses. By late 2023, initial commissioning accelerated the beam through the early NC sections to about 74 MeV.

For high-power accelerators such as ESS, the beam phase, defined as the phase of the beam relative to the accelerating rf field, is a critical quantity for stable operation and loss mitigation. Conventional calibration relies on direct phase-scan techniques, including the $\Delta T$ phase scan [4–7] and phase-scan signature matching [7,8]. In these methods, the rf phase of a selected cavity is varied

TABLE I. ESS linac high-level parameters [2].

| Parameter | Unit | Value |
|---|---|---|
| Beam power | MW | 5 |
| Beam energy | GeV | 2 |
| Peak beam current | mA | 62.5 |
| Beam pulse length | ms | 2.86 |
| Pulse repetition rate | Hz | 14 |
| Duty factor | % | 4 |
| rf frequency | MHz | 352.21/704.42 |
| Availability | % | 95 |

*Contact author: qiufeng@impcas.ac.cn
†Contact author: hey@impcas.ac.cn

*Published by the American Physical Society under the terms of the Creative Commons Attribution 4.0 International license. Further distribution of this work must maintain attribution to the author(s) and the published article's title, journal citation, and DOI.*

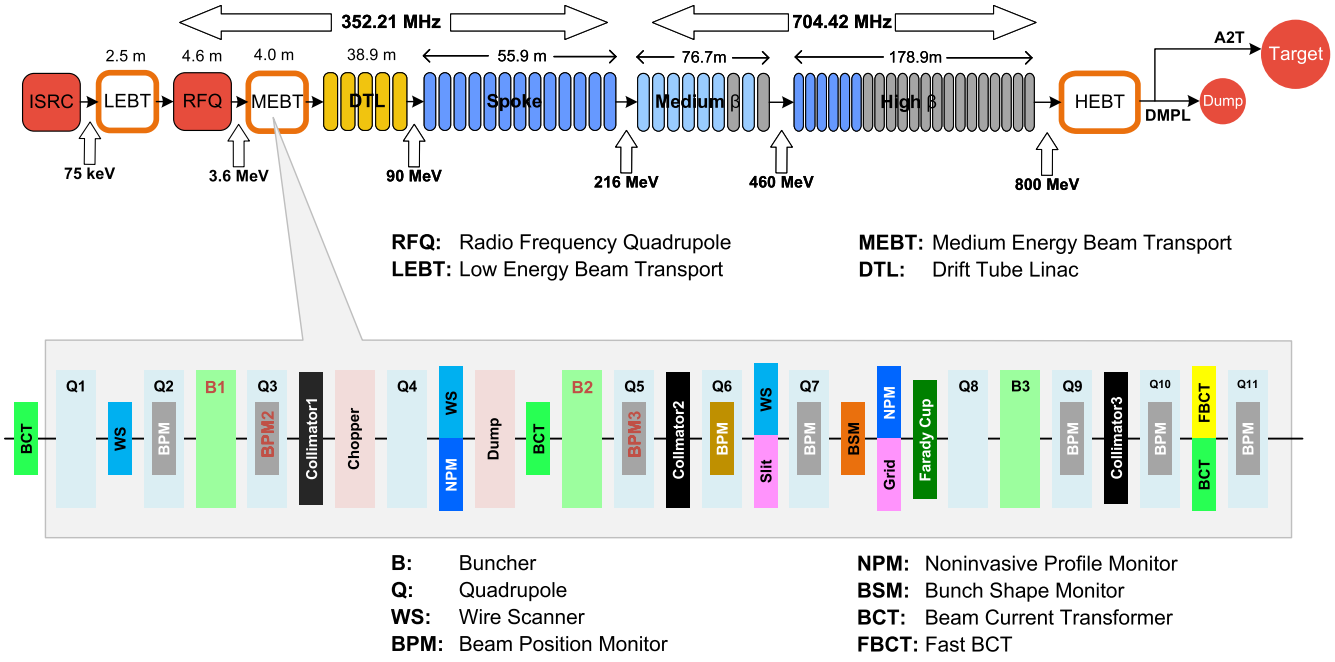



FIG. 1. Schematic layout of the ESS linac for 800 MeV and 2 MW operation (top) and a detailed view of the MEBT section (bottom) [2]. Each segment in the top panel represents a DTL tank or a cryomodule, with gray-shaded units remaining unpowered during initial operation. The bottom panel illustrates the matching optics and diagnostics of the MEBT. This study primarily employs buncher cavities B1 and B2, along with two BPMs (BPM2 and BPM3) integrated within the quadrupole magnets Q3 and Q5, respectively (labels indicated in red in the bottom panel).

while monitoring the downstream response. They are effective but intrusive, consuming dedicated beamtime and typically performed off-line during commissioning or maintenance. Periodic recalibration remains necessary during routine operation due to slow drifts in the beam diagnostic systems.

Indirect measurement techniques based on rf signals have been explored. The drifting-beam method at SNS infers the relative beam phase from LLRF measurements of beam-induced rf transients in an unpowered SC cavity [9]. However, relying on unpowered cavities is inherently inefficient, as these cavities cannot contribute to beam acceleration. At DESY, a short beam pulse in a powered SC cavity generates an in-phase/quadrature (I/Q) transient whose trajectory is fitted linearly to extract the phase [10–13], enabling online measurement. This approach effectively avoids the influence of drifts in the diagnostic systems; nonetheless, it typically assumes open-loop cavity operation.

For high-current proton linacs such as ESS, operating the cavity without feedback poses significant safety and practical challenges. Open-loop operation is unsuitable due to elevated risks of beam loss and trips [14–17]. Therefore, it is preferable to ensure that the LLRF system operates in the closed-loop (CL) mode during measurements.

To address online measurement challenges under CL constraints, several strategies have been investigated. Building upon open-loop techniques, DESY demonstrated a closed-loop calibration method that evaluates the beam-induced voltage $\mathbf{V}_b$ by solving the cavity differential equation [18]. However, its reliance on the numerical derivative of the cavity voltage ($d\mathbf{V}_c/dt$) inherently amplifies high-frequency noise, especially in low-current scenarios. This necessitates a difficult trade-off between noise mitigation via digital filtering and the risk of signal distortion.

Another strategy utilizes the beam-induced transient signal exclusively within the loop-delay ($T_d$) window [19], hereafter referred to as the CL method. By analyzing the transient before feedback takes effect, this method enables online beam-phase determination during closed-loop operation. Nevertheless, its precision is fundamentally limited by the microsecond-level loop delay of modern LLRF systems, which provides insufficient sampling points. Our experiments at ESS confirmed this limitation, observing phase errors of up to $\approx 2°$ using this approach [19].

To further enhance measurement precision and leverage the information available across the entire beam pulse, this paper presents two complementary schemes designed for high-accuracy closed-loop diagnostics.

The first is the virtual open-loop (VOL) method. While sharing a mathematical foundation with Ref. [18], the VOL method isolates the beam-loading contribution by iteratively solving the discrete-time cavity difference equation to subtract control-loop effects. By bypassing the direct calculation of the numerical derivative $d\mathbf{V}_c/dt$,

this approach provides a more robust approach for maintaining precision in low-current scenarios. Furthermore, the ability of the VOL method to reconstruct time-domain waveforms facilitates an intuitive comparison with traditional open-loop measurements, which is highly beneficial for system debugging during commissioning.

The second is the steady-state (SS) method. This approach is applicable to scenarios involving long macropulses, where the forward power reaches a steady state and the cavity voltage remains stable during beam passage. Provided that both beam loading and dynamic detuning are effectively compensated by the low-level radio-frequency (LLRF) system, the beam parameters can be accurately inferred from the vector difference between the steady-state forward voltages measured with and without the beam. Although the SS principle was preliminarily tested at the CAFe facility [20,21], this work presents a systematic performance validation on the ESS NC buncher cavities, including a comprehensive benchmark against the VOL method.

The proposed VOL and SS schemes complement traditional phase scans by providing a nonintrusive, real-time layer for tracking phase and voltage drifts. While beam position monitors (BPMs) are standard diagnostics, these LLRF-based methods leverage existing infrastructure to provide an independent physical reference at every cavity without additional hardware investment. This capability is particularly valuable for online detection during the operational phase and rapid fault localization, while also enhancing the overall diagnostic observability during early commissioning, even under weak beam-loading conditions (see the Appendix for the VOL implementation in such scenarios). Both approaches were systematically validated on the ESS buncher cavity, showing agreement with independent beam diagnostics, with phase error within $\pm 0.5°$ and current error within $\pm 4\%$.

The remainder of this paper is organized as follows. Sections II and III detail the fundamental principles of the VOL and SS methods, respectively. Section IV reports on the experimental setup and the measurement results obtained from the ESS linac buncher cavities. Section V provides a comparative discussion of the operational applicability of these two methods, followed by a dedicated quantitative analysis of their systematic uncertainties. Finally, Sec. VI concludes the paper and outlines potential directions for future work. The Appendix details the mathematical generalization of the VOL method to time-varying SRF systems, supplemented by experimental validation from the real facility.

## II. PRINCIPLES OF THE VIRTUAL OPEN-LOOP METHOD

When a beam pulse enters an rf cavity operating in open loop, the change in $\mathbf{V}_c$ will follow a specific path in the I/Q plane. As shown in Figs. 2(a) and 2(b), the initial direction (slope) of this transient trajectory is directly determined by the beam phase $\varphi_b$ relative to the rf field. This is the method proposed by DESY for measuring beam phase in open-loop mode.

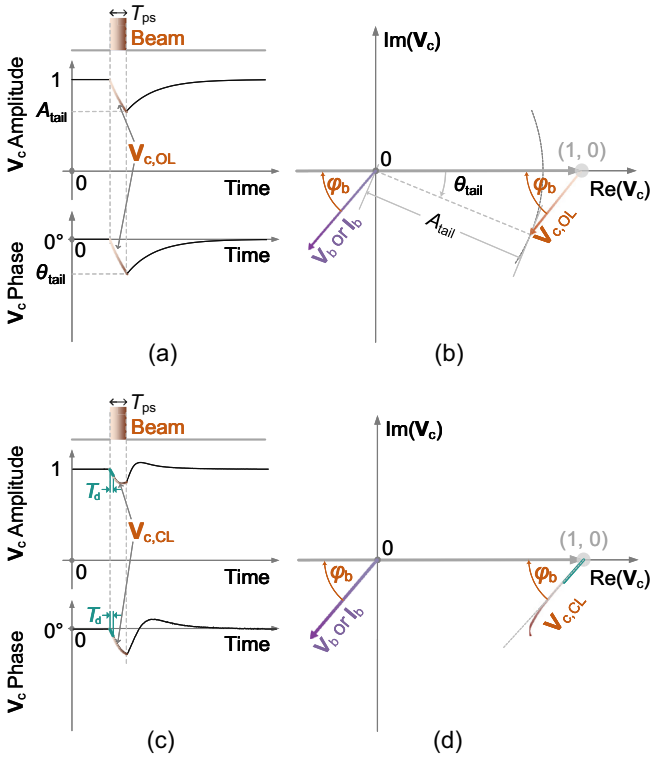



FIG. 2. Principles of beam-phase measurement using beam-induced rf transients. (a) Time-domain evolution and (b) I/Q trajectory for the open-loop (OL) DESY method, where the initial transient direction of $\mathbf{V}_{c,OL}(t)$ reflects $\varphi_b$. (c) Time-domain principle and (d) I/Q trajectory for the $T_d$-based closed-loop (CL) method, where $\varphi_b$ is inferred from the initial trajectory within the loop delay ($T_d$) before feedback activates.

As established in the Introduction, this open-loop operation is not practical or safe for high-current proton linacs such as ESS [14,15]. A foundational strategy for adapting this technique to closed-loop operation is to exploit the system's loop delay ($T_d$), as proposed in Ref. [19]. This principle is illustrated in Figs. 2(c) and 2(d). Within the brief time window $t < T_d$ (typically on the order of $\approx 1.4\,\mu s$), the feedback system has not yet begun to correct for the beam-induced field change. Consequently, the initial transient trajectory is identical to the open-loop case, allowing $\varphi_b$ to be inferred. However, as noted in the Introduction, the CL method's precision is inherently constrained by the small number of sampling points available within this short analysis window [19].

To overcome this fundamental constraint imposed by $T_d$, we propose the VOL method. The central idea of this approach is to mathematically reconstruct the "pure" beam-induced transient signal as if the feedback loop were open, even while the loop is fully closed and active (i.e., for $t > T_d$).

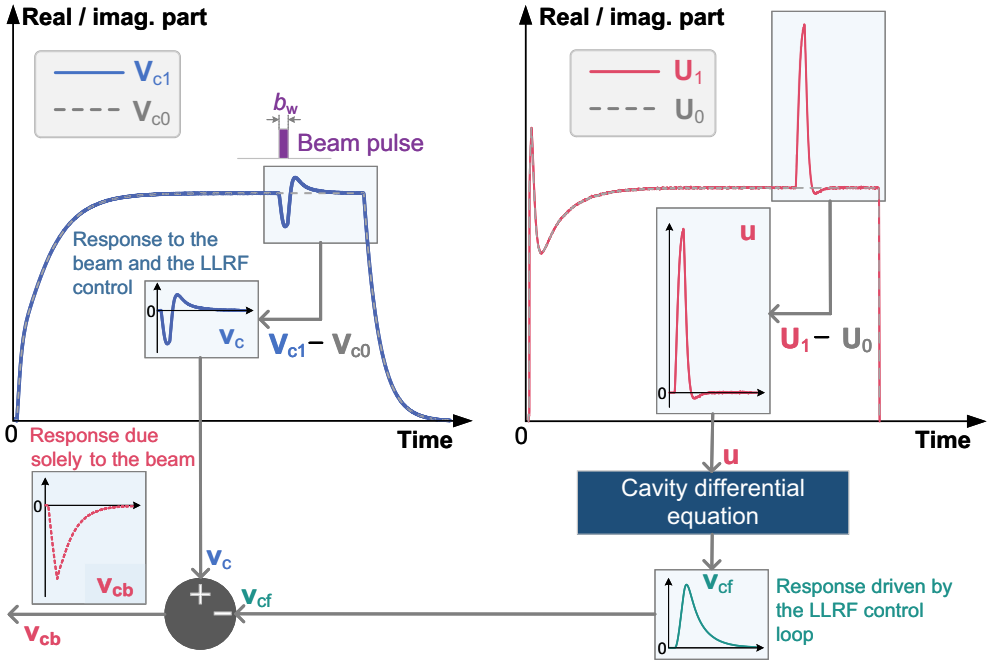



FIG. 3. Principle of the VOL method. The total measured voltage variation $\mathbf{v}_c$ (derived from $\mathbf{V}_{c1}$ and $\mathbf{V}_{c0}$) is the superposition of the desired "pure" beam response $\mathbf{v}_{cb}$ and the loop-driven response $\mathbf{v}_{cf}$. The VOL algorithm (right panel) calculates $\mathbf{v}_{cf}$ by feeding the differential forward signal $\mathbf{u}$ (derived from $\mathbf{V}_{f1}$ and $\mathbf{V}_{f0}$) into the cavity differential equation model. The VOL response $\mathbf{v}_{cb}$ is then isolated via subtraction ($\mathbf{v}_c - \mathbf{v}_{cf}$). All signals are complex (I/Q) quantities; for schematic simplicity, traces show only one component (e.g., the real part).

The principle of the VOL algorithm, illustrated in Fig. 3, is to numerically separate the total measured voltage variation $\mathbf{v}_c$ into a loop-driven component $\mathbf{v}_{cf}$ and the desired beam-loading component $\mathbf{v}_{cb}$. The theoretical basis for this separation is the standard differential equation governing the cavity field [22–25], which is used to compare the system dynamics between a reference pulse without beam ($\mathbf{V}_{c0}$) and an adjacent pulse with beam ($\mathbf{V}_{c1}$). Throughout this paper, boldface symbols (e.g., $\mathbf{V}_c$, $\mathbf{I}_b$) denote complex-valued (I/Q) quantities. These two pulse dynamics are governed by

$$\begin{aligned}\frac{d\mathbf{V}_{c0}}{dt} + (\omega_{0.5} - j\Delta\omega)\mathbf{V}_{c0} &= \omega_{0.5}\frac{2\beta}{1+\beta}\mathbf{V}_{f0}(t)\\ \frac{d\mathbf{V}_{c1}}{dt} + (\omega_{0.5} - j\Delta\omega)\mathbf{V}_{c1} &= \omega_{0.5}\frac{2\beta}{1+\beta}\mathbf{V}_{f1}(t) + \omega_{0.5}\mathbf{V}_b(t).\end{aligned} \tag{1}$$

Here, $\mathbf{V}_c$ (used in $\mathbf{V}_{c0}$, $\mathbf{V}_{c1}$) and $\mathbf{V}_f$ (used in $\mathbf{V}_{f0}$, $\mathbf{V}_{f1}$) are the calibrated cavity and forward voltages, respectively. These physical quantities are derived from the raw LLRF measurements (e.g., $\mathbf{V}_f^*$ and $\mathbf{V}_r^*$) [20,22,23,26,27]. For instance, the calibrated cavity voltage is reconstructed as

$$\mathbf{V}_c = X\mathbf{V}_f^* + Y\mathbf{V}_r^*, \tag{2}$$

where $X$ and $Y$ are complex calibration coefficients that can be obtained via linear regression [20,22,23,26,27]. In Eq. (1), $\omega_{0.5}$ is the cavity half-bandwidth, $\Delta\omega$ is the detuning (assumed constant for both pulses), $\beta$ is the coupling coefficient, and $\mathbf{V}_b$ is the equivalent voltage induced by the beam current $\mathbf{I}_b$ (where $\mathbf{V}_b = R_L\mathbf{I}_b$, with $R_L$ being the loaded shunt impedance).

To simplify the derivation, we define the scaled forward voltage as $\mathbf{U}(t) = \frac{2\beta}{1+\beta}\mathbf{V}_f(t)$. We denote the scaled voltages for the two pulses as $\mathbf{U}_1 = \frac{2\beta}{1+\beta}\mathbf{V}_{f1}$ and $\mathbf{U}_0 = \frac{2\beta}{1+\beta}\mathbf{V}_{f0}$. Let $\mathbf{v}_c = \mathbf{V}_{c1} - \mathbf{V}_{c0}$ and $\mathbf{u} = \mathbf{U}_1 - \mathbf{U}_0$. By subtracting Eq. (1) for the two pulses, we obtain

$$\frac{d\mathbf{v}_c}{dt} + (\omega_{0.5} - j\Delta\omega)\mathbf{v}_c = \underbrace{\omega_{0.5}\mathbf{u}}_{\text{loop drive}} + \underbrace{\omega_{0.5}\mathbf{V}_b}_{\text{beam loading}}. \tag{3}$$

The input term on the right-hand side of Eq. (3) consists of two parts: The first part is the rf loop drive term, which represents the forward voltage term from the rf power source, as adjusted by the rf loop. The second part is the beam-loading term. The $\mathbf{v}_c$ in the differential equation represents the cavity voltage variation under the combined effect of the rf loop drive term and the beam-loading term.

It should be noted that the primary experimental validation in this study was conducted on an NC buncher cavity, where the prebeam cavity voltage ($\mathbf{V}_{c0}$), forward voltage ($\mathbf{V}_{f0}$), and cavity detuning typically reach a stable steady state. In such NC cavities, the high mechanical stiffness renders Lorentz-force-induced detuning (LFD)

negligible. Introducing the differential variables ($\mathbf{v}_c$ and $\mathbf{u}$) in this context helps eliminate the steady-state baseline and suppress common-mode noise, thereby facilitating a more precise and effective extraction of the beam-loading response. While these steady-state assumptions simplify the present derivation, the VOL concept is inherently adaptable to more complex scenarios, including SC radio-frequency (SRF) cavities characterized by large time constants and significant dynamic LFD, as well as low-current regimes where the beam-induced signal is relatively weak. A more generalized formulation incorporating time-varying parameters, such as $\Delta\omega(t)$ and nonsteady $\mathbf{V}_f$ baselines, is detailed in the Appendix.

Following the definition of these differential variables, the specific mathematical procedure for isolating the beam-loading response is implemented as follows.

To isolate the beam-loading response, we must first calculate the response driven by the loop. Let $\mathbf{v}_{cf}$ be the cavity voltage variation caused only by the loop drive term $\mathbf{u}$. This component is governed by

$$\frac{d\mathbf{v}_{cf}}{dt} + (\omega_{0.5} - j\Delta\omega)\mathbf{v}_{cf} = \omega_{0.5}\mathbf{u}, \tag{4}$$

where $\mathbf{v}_{cf}$ is the cavity voltage variation caused by the loop drive term $\mathbf{u}$.

Using a first-order finite-difference approximation, we write

$$\frac{d\mathbf{v}_{cf}}{dt} \approx \frac{\mathbf{v}_{cf}(n+1) - \mathbf{v}_{cf}(n)}{T_s}, \tag{5}$$

where $T_s$ is the sampling period. Substituting this into Eq. (4) and rearranging for $\mathbf{v}_{cf}(n+1)$ gives:

$$\mathbf{v}_{cf}(n+1) = \mathbf{v}_{cf}(n) - T_s(\omega_{0.5} - j\Delta\omega)\mathbf{v}_{cf}(n) + T_s\omega_{0.5}\mathbf{u}(n).$$

By expanding this complex equation into its real (I) and imaginary (Q) components, we obtain the state-space representation:

$$\begin{bmatrix} v_{cf,i}(n+1) \\ v_{cf,q}(n+1) \end{bmatrix} = \begin{bmatrix} 1 - T_s\omega_{0.5} & -T_s\Delta\omega \\ T_s\Delta\omega & 1 - T_s\omega_{0.5} \end{bmatrix} \begin{bmatrix} v_{cf,i}(n) \\ v_{cf,q}(n) \end{bmatrix} + \begin{bmatrix} T_s\omega_{0.5} & 0 \\ 0 & T_s\omega_{0.5} \end{bmatrix} \begin{bmatrix} u_i(n) \\ u_q(n) \end{bmatrix}. \tag{6}$$

Here, $v_{cf,i}$ and $v_{cf,q}$ are the I and Q components of $\mathbf{v}_{cf}$, and $u_i$ and $u_q$ are the I and Q components of $\mathbf{u}$. $T_s$ is the sampling period for the signals.

By solving the difference equation (6) iteratively, the cavity voltage variation $\mathbf{v}_{cf}$ (caused by the loop drive term) is obtained. Since the differential Eq. (3) is linear, the voltage variation induced by the beam-loading term, $\mathbf{v}_{cb}$, is isolated by subtracting $\mathbf{v}_{cf}$ from the total variation $\mathbf{v}_c$. This $\mathbf{v}_{cb}$ is then added to the no-beam cavity voltage $\mathbf{V}_{c0}$ to reconstruct the cavity signal $\mathbf{V}_{c,\,VOL}$, which contains only the beam-loading term (not the loop drive term). This

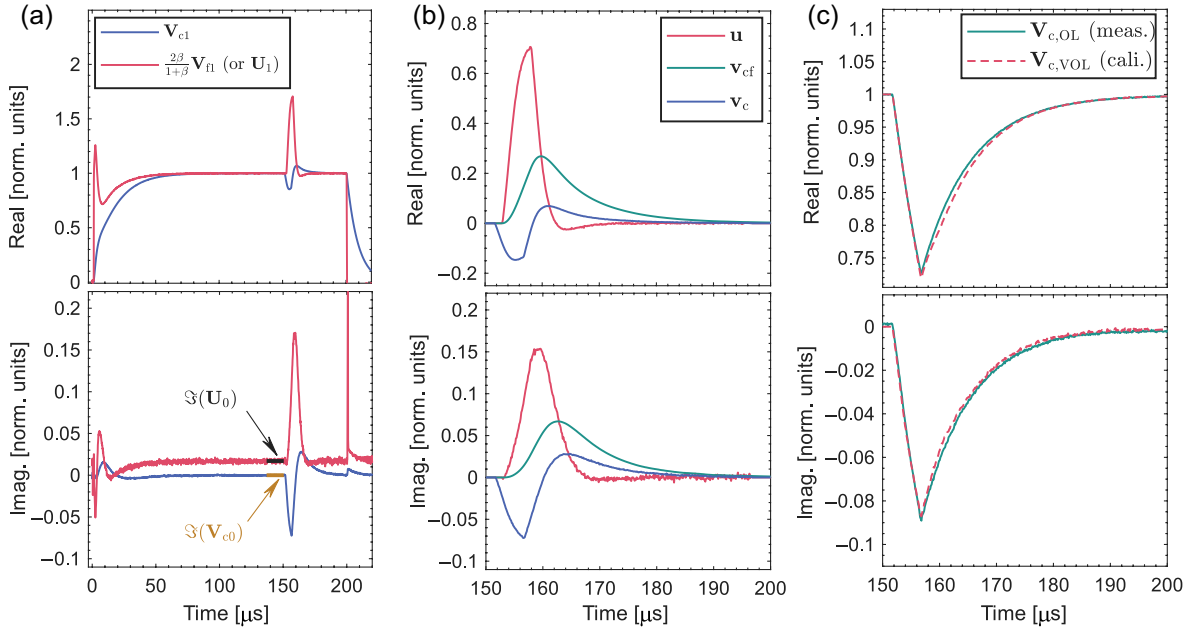



FIG. 4. An example of the VOL signal reconstruction from experimental data (60 mA, −19°). (a) Measured signals for the pulse with beam (cavity voltage $\mathbf{V}_{c1}$ and scaled forward voltage $\mathbf{U}_1$). (b) Decomposition of the differential signals during the beam transient (150–200 μs): the total measured variation $\mathbf{v}_c$, the loop drive term $\mathbf{u}$, and the calculated loop-driven response $\mathbf{v}_{cf}$. (c) Comparison of the final reconstructed $\mathbf{V}_{c,\,VOL}$ with the actual measured open-loop response $\mathbf{V}_{c,OL}$, demonstrating the method's accuracy.

$\mathbf{V}_{\mathrm{c,\,VOL}}$ signal no longer contains the contribution from the rf control loop and can thus be regarded as the beam-induced cavity signal under "virtual open-loop" conditions. This process is formulated as follows:

$$\mathbf{v}_{\mathrm{cb}}(n) = \mathbf{v}_{\mathrm{c}}(n) - \mathbf{v}_{\mathrm{cf}}(n) \tag{7}$$

$$\mathbf{V}_{\mathrm{c,\,VOL}}(n) = \mathbf{V}_{\mathrm{C0}} + \mathbf{v}_{\mathrm{cb}}(n). \tag{8}$$

The practical application and validity of this VOL reconstruction algorithm are demonstrated in Fig. 4 using experimental data from an ESS buncher cavity. In each panel (a), (b), and (c), all complex I/Q signals are shown with the real part (I) plotted in the top trace and the imaginary part (Q) in the bottom trace. Figure 4(a) displays the raw measured signals for the pulse with beam, $\mathbf{V}_{\mathrm{c1}}$ and the scaled forward voltage $\mathbf{U}_1$. Moreover, as seen in Fig. 4(a), during routine closed-loop operation, the rf signals, including the cavity detuning, settle before beam arrival; therefore $\mathbf{V}_{\mathrm{c0}}$ and $\mathbf{U}_0$ may be taken from the prebeam subwindow of the same pulse. This substitution improves operational flexibility by removing the need for a dedicated no-beam pulse. A detailed discussion is given in Sec. III. Following the subtraction of the no-beam reference pulse, the resulting differential signals are decomposed in Fig. 4(b). This panel explicitly shows the total measured variation $\mathbf{v}_{\mathrm{c}}$, the LLRF control loop drive term $\mathbf{u}$ (as defined for Eq. (4), and the loop-driven response $\mathbf{v}_{\mathrm{cf}}$ computed by numerically solving the cavity difference equation [Eq. (6)]. The "pure" beam-loading component $\mathbf{v}_{\mathrm{cb}}$ is then isolated using Eq. (7), and the complete VOL signal $\mathbf{V}_{\mathrm{c,VOL}}$ is reconstructed via Eq. (8). As shown in Fig. 4(c), this reconstructed $\mathbf{V}_{\mathrm{c,VOL}}$ agrees closely with the measured open-loop response $\mathbf{V}_{\mathrm{c,OL}}$ under the same beam conditions, which confirms that the algorithm successfully subtracts the closed-loop control actions and isolates the beam-induced rf transient.

With $\mathbf{V}_{\mathrm{c,VOL}}$ available, the beam phase can be determined using the DESY open-loop transient method as shown in Figs. 2(a) and 2(b) [10,11,13,18]. In the I–Q plane, the angle between $\mathbf{V}_{\mathrm{c,VOL}}$ and the negative I axis equals the synchronous beam phase, which we compute as

$$\varphi_{\mathrm{b}} = 180^\circ - \angle \mathbf{V}_{\mathrm{c,VOL}}. \tag{9}$$

The vector magnitude $|\mathbf{V}_{\mathrm{c,VOL}}|$ also carries information on the beam-current amplitude.

These estimates (beam current and phase) are influenced by cavity detuning: for SC cavities, where the filling time constant is large, the effect is usually small, whereas for NC cavities, a correction is required. Here, we briefly illustrate this using Fig. 5: in the I/Q plane, cavity detuning (i.e., the case $\Delta\theta \neq 0°$) causes the I/Q trajectory of the beam-induced rf transient to rotate relative to the true beam

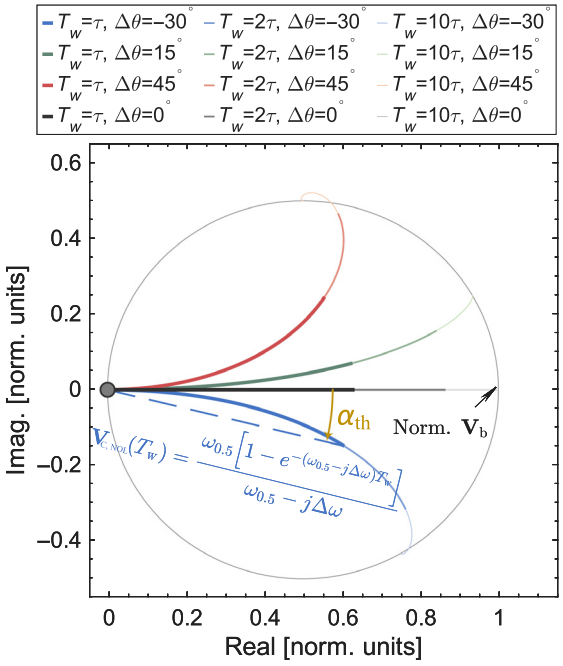



FIG. 5. Simulation illustrating the effect of detuning angle ($\Delta\theta$) on the I/Q trajectory of the VOL method. The plot shows the path of the normalized beam-induced transient vector $\mathbf{V}_{\mathrm{C,NOL}}(T_w)$ under open-loop operation for various detuning angles and calibration window durations ($T_{\mathrm{w}}$). In the legend, $\tau$ denotes the cavity time constant, $\tau = 1/\omega_{0.5}$. Detuning ($\Delta\theta \neq 0°$) causes the trajectory to rotate by an angle $\alpha_{\mathrm{th}}$ away from the true phase (represented by the normalized $\mathbf{V_b}$ vector). This deflection $\alpha_{\mathrm{th}}$ depends on both $T_{\mathrm{w}}$ and $\Delta\theta$, necessitating the detuning calibration for the VOL method.

phase (represented by the "Norm. $\mathbf{V}_{\mathrm{b}}$" vector). This rotation introduces a deflection angle $\alpha_{th}$, the magnitude of which depends on both the detuning angle $\Delta\theta$ and the calibration time window $T_{\mathrm{w}}$. The mathematical expression for the normalized I/Q trajectory (with $\mathbf{V}_{\mathrm{b}}$ normalized to 1 + 0j) is:

$$\mathbf{V}_{\mathrm{c,\,NOL}}(T_w) = \frac{\omega_{0.5}[1 - e^{-(\omega_{0.5} - j\Delta\omega)T_w}]}{\omega_{0.5} - j\Delta\omega}. \tag{10}$$

Therefore, to obtain an accurate phase estimate, this detuning-induced rotation must be calibrated. The procedure is described in detail in Ref. [19]. The consequence of omitting this correction will be illustrated in Sec. V.

Based on Eq. (10) and Fig. 5, the calculation formula for $\mathbf{V}_{\mathrm{b}}$ (which relates the measured $\mathbf{V}_{\mathrm{c,VOL}}$ to the normalized response) is:

$$\mathbf{V}_{\mathrm{b}} = \frac{1}{\mathbf{V}_{\mathrm{c,\,NOL}}(T_{\mathrm{w}})}\,\mathbf{V}_{\mathrm{c,\,VOL}}(T_{\mathrm{w}}). \tag{11}$$

Finally, the dc beam current $I_{\mathrm{b0}}$ ($I_{\mathrm{b0}} = 0.5|\mathbf{I}_{\mathrm{b}}|$) and beam phase $\varphi_b$ can be derived from $\mathbf{V}_{\mathrm{b}}$. Using the loaded shunt impedance $R_{\mathrm{L}} = \frac{1}{2}(r/Q)Q_{\mathrm{L}}$ and the calibration gain

$G$ that maps the normalized cavity voltage to the physical value, we write

$$I_{b0} = \frac{G|\mathbf{V}_b|}{(r/Q)Q_L}, \qquad \varphi_b = 180° - \angle \mathbf{V}_b. \tag{12}$$

Here $(r/Q)$ is the cavity geometric parameter and $Q_L$ is the loaded cavity quality factor.

## III. PRINCIPLES OF THE STEADY-STATE METHOD

The "steady-state" (SS) method applies when the LLRF system enforces the constant-voltage condition $\mathbf{V}_{c1} \approx \mathbf{V}_{c0}$ via feedback and feedforward control (e.g., ILC). While absolute equality is physically unattainable, a residual deviation within 0.5% is generally achievable in modern digital LLRF systems within a given time window (typically excluding the steep rising and falling edges of the beam pulse). Such precision ensures that the resulting bias in the $\mathbf{V}_b$ calibration remains within the same order of magnitude. According to Eq. (1), subtracting the no-beam equation from the with-beam equation over the same window gives

$$\omega_{0.5}(\mathbf{U}_1 - \mathbf{U}_0) + \omega_{0.5}\mathbf{V}_b = 0 \Rightarrow \mathbf{V}_b = \mathbf{U}_0 - \mathbf{U}_1,$$

where $\mathbf{U}_1$ and $\mathbf{U}_0$ denote the scaled forward voltages for the with-beam and no-beam cases, evaluated over the same beam-passage window. Operationally, computing $\mathbf{V}_b$ requires recording the rf forward signal for two consecutive pulses—first without beam and then with beam—which inevitably introduces a modest perturbation to routine beam operation.

In practice, if the detuning is approximately constant within the rf-pulse flattop, $\Delta\omega(t) \approx \Delta\omega_0$ for $t \in \mathcal{W}_{flat}$ [see Fig. 6(a)], the measurement can be completed within a single beam pulse. This condition is typically satisfied for NC cavities; for SC cavities, it can be met using an active fast tuner (e.g., a piezoelectric tuner) to compensate for the dynamic LFD. Within the same flattop, choose a prebeam or postbeam subwindow free of transients as the no-beam reference $\mathbf{U}_p$, and the beam-passage (during beam) subwindow as $\mathbf{U}_d$ [Fig. 6(a)]. The phasor construction in Fig. 6(b) then yields

$$\mathbf{V}_b = \mathbf{U}_p - \mathbf{U}_d, \tag{13}$$

where the chord from $\mathbf{U}_p$ to $\mathbf{U}_d$ corresponds to $-\mathbf{V}_b$. This single-pulse protocol avoids pulse-to-pulse switching and minimizes operational perturbation, provided the LLRF holds $\mathbf{V}_c$ flat across both subwindows.

A key advantage of the SS method relative to the VOL method is its robustness against cavity detuning. Building on the single-pulse construction, we validated this feature

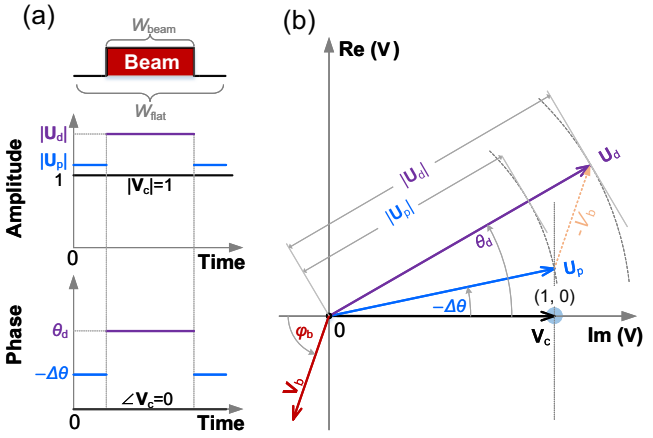



FIG. 6. Principle of the steady-state (SS) beam measurement method. (a) Time-domain waveforms illustrating that the LLRF system, through feedback and/or feedforward (e.g., constant or ILC-based FF) control, maintains a constant cavity voltage $\mathbf{V_c}$ (normalized to 1 + 0j). (b) The corresponding phasor diagram, showing that the required forward drive $\mathbf{U_p}$ (pre-post beam) is changed to $\mathbf{U_d}$ (during beam) to keep $\mathbf{V_c}$ constant. As derived in Ref. [20], this change in drive ($\mathbf{U_p} - \mathbf{U_d}$) reflects the beam-induced voltage $\mathbf{V_b}$. Consequently, the beam current and phase can be inferred from the amplitude and phase angle of the vector $\mathbf{V_b}$, respectively.

on an NC buncher cavity at ESS. Two representative detuning scenarios were examined: small detuning (case 1, $\Delta\theta \approx 15°$) and large detuning (case 2, $\Delta\theta \approx 60°$). Figure7(a) shows that the LLRF held the cavity field $\mathbf{V}_c$ approximately constant under full compensation, with residual variations restricted to less than 0.2% over the measurement window (typically excluding the steep rising and falling edges of the beam pulse). Figure 7(b) shows the scaled forward drive $\mathbf{U}(t)$, from which we extracted the "during-beam" samples $(\mathbf{U}_{d1}, \mathbf{U}_{d2})$ and the "post-beam" samples $(\mathbf{U}_{p1}, \mathbf{U}_{p2})$ within the same flattop window. The phasor diagram in Fig. 7(c) then indicates that the beam-induced voltages $\mathbf{V}_{b1,b2}$ computed via Eq. (13) (i.e., $\mathbf{V}_b = \mathbf{U}_p - \mathbf{U}_d$) are consistent for both cases, demonstrating that the SS method is robust against the cavity detuning. Once $\mathbf{V}_b$ is known, $I_{b0}$ and $\varphi_b$ can be determined using Eq. (12).

## IV. EXPERIMENTAL VALIDATION

Having established the principles of the VOL and SS approaches, we conducted follow-up measurements on the ESS MEBT normal-conducting buncher cavities B1 and B2 (Fig. 1) to evaluate their performance under realistic conditions. Two pulse-length settings were used, $T_{ps} =$ 5 μs and 50 μs, and the beam current and synchronous phase were adjusted as required to span the operating range. Beam current and phase were independently monitored by beam current transformers (BCTs) and by two

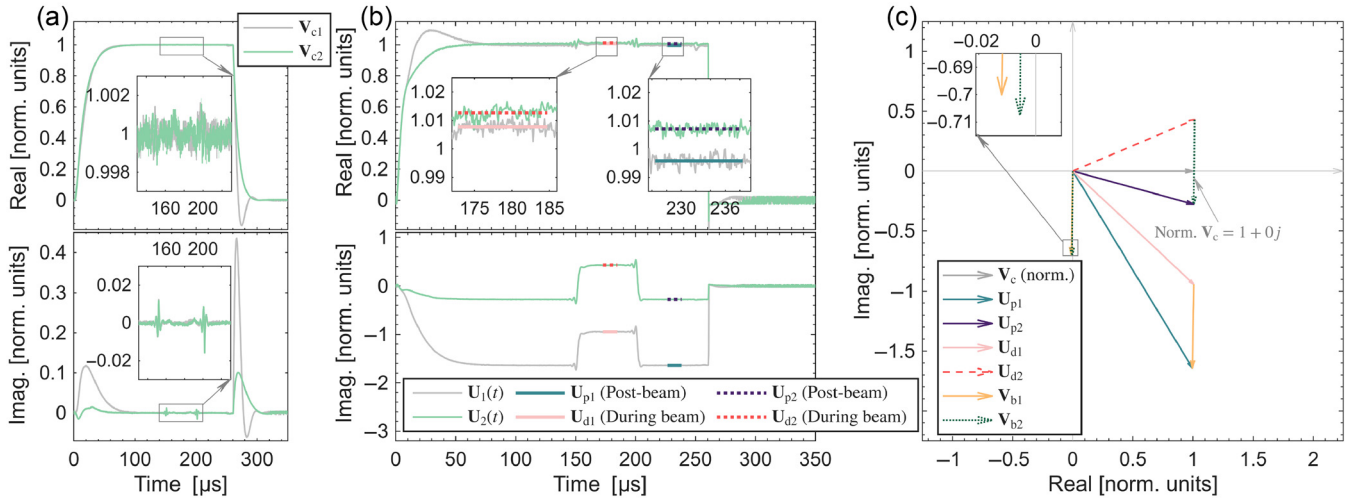



FIG. 7. Experimental results of the steady-state (SS) method for two cases: small detuning (case 1, $\Delta\theta \approx 15°$) and large detuning (case 2, $\Delta\theta \approx 60°$). (a) Cavity voltage ($\mathbf{V}_{c1,\,c2}$) showing full beam-loading compensation by the FB + FF system. (b) Drive signals for "during beam" ($\mathbf{U}_{d1,\,d2}$) and "post-beam" ($\mathbf{U}_{p1,\,p2}$) states, extracted from the scaled forward signals $\mathbf{U}_{1,2}(t)$. (c) Phasor diagram, referenced to $\mathbf{V}_c = (1 + 0j)$, showing the beam-induced voltage $\mathbf{V}_{b1,b2}$ derived from the vector difference (e.g., $\mathbf{V}_{b1} \approx \mathbf{U}_{p1} - \mathbf{U}_{d1}$). The result validates the SS principle and demonstrates its robustness against the cavity detuning.

BPMs (BPM2 and BPM3) located in Q3 and Q5 (Fig. 1). The reference beam current and phase profiles measured by these diagnostics are shown in Fig. 8. We also observe in Fig. 8 that the high-current beam exhibits an intrapulse phase variation of approximately 2°. The influence of this fluctuation will be quantified in the subsequent analysis. Representative rf pulse waveforms corresponding to these beam conditions are shown in Fig. 9, and the principal rf parameters are summarized in Table II; together these characterize the experimental conditions for assessing the VOL and SS methods.

### A. Validation of the VOL method

We first characterize the experimental conditions under different control schemes using a 60 mA beam, with results shown in Fig. 9. The figure compares the measured cavity voltage ($\mathbf{V_c}$) and forward voltage ($\mathbf{V_f}$) for two beam pulse widths: 5 μs [Figs. 9(a) and 9(b)] and 50 μs [Figs. 9(c) and 9(d)]. Three control modes are shown: "open loop" (green), "only CL" (red), and "CL + ILC-FF" (black). While the 5 μs case allows a direct comparison of all three modes, the 50 μs "open loop" case is not presented; as noted in the caption, operating under these

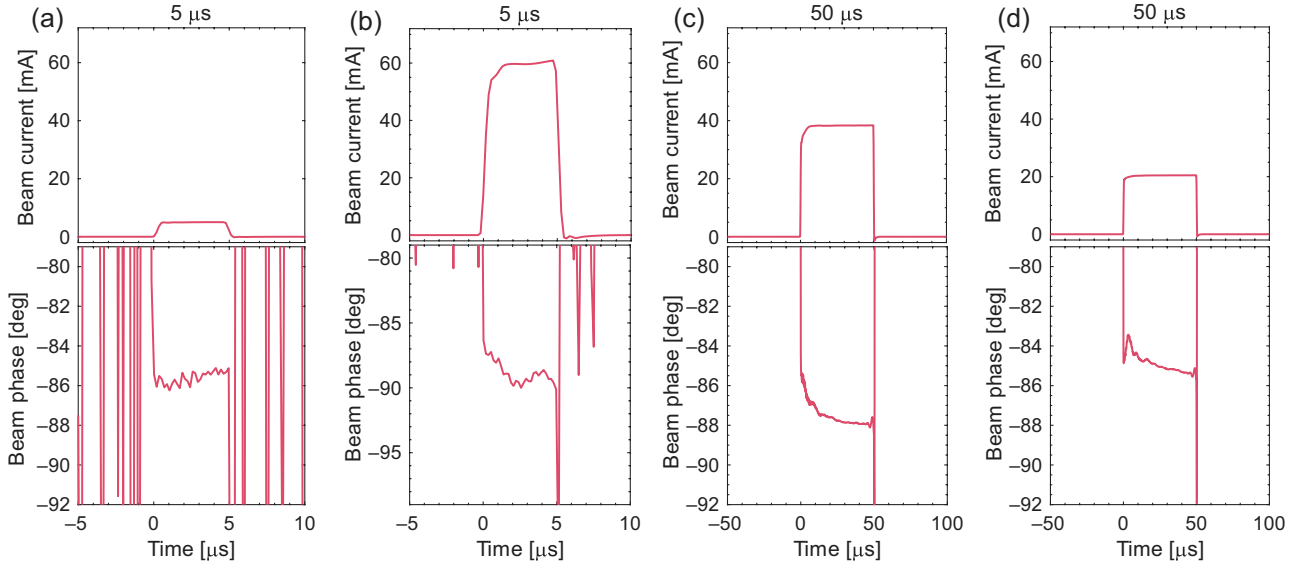



FIG. 8. Reference beam current (top panels) and phase (bottom panels) profiles measured by the independent beam diagnostics (BCT/BPM) for the $T_{ps} = 5\,\mu s$ (a),(b) and $T_{ps} = 50\,\mu s$ (c),(d) cases. These measurements serve as the ground truth for validating the rf-based VOL and SS methods.

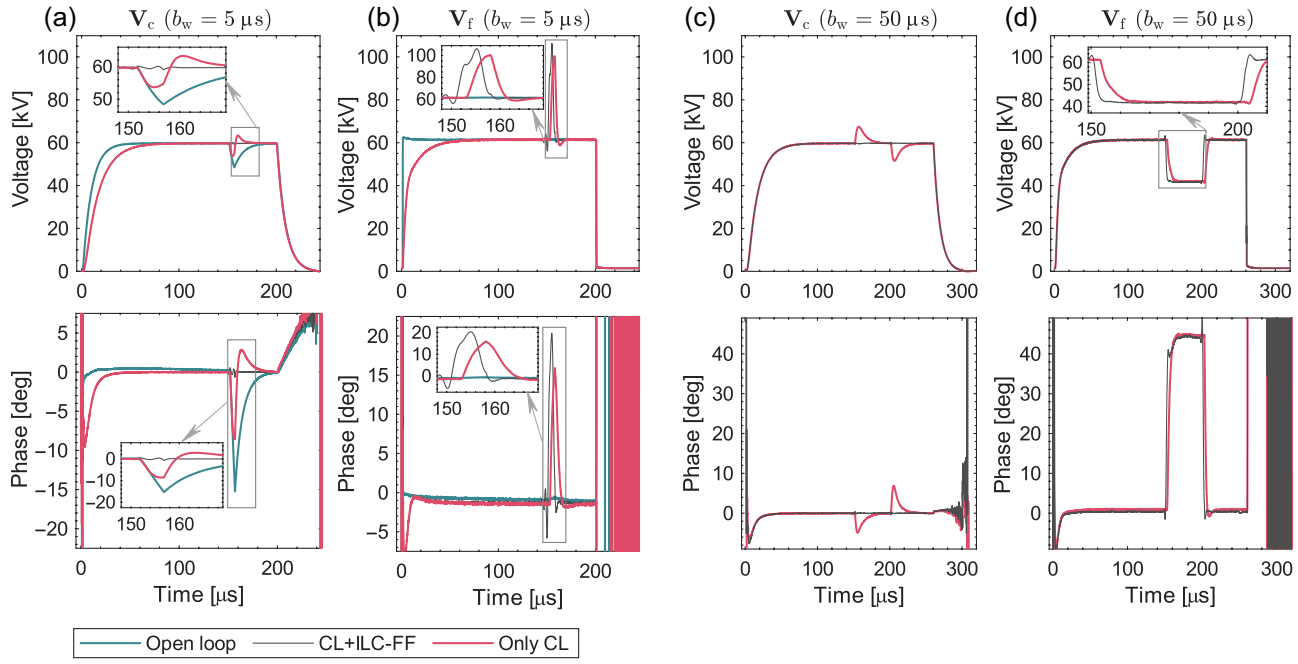



FIG. 9. Comparison of cavity voltage ($\mathbf{V_c}$) and forward voltage ($\mathbf{V_f}$) under three different control modes for a 60 mA beam. (a) $\mathbf{V_c}$ and (b) $\mathbf{V_f}$ for a short, 5 μs beam pulse. (c) $\mathbf{V_c}$ and (d) $\mathbf{V_f}$ for a long, 50 μs beam pulse. The control modes compared are as follows: "open loop" (green), "only CL" (closed-loop without feedforward, red), and "CL + ILC-FF" (closed-loop with iterative learning control feedforward, black). Note that the 50 μs, 60 mA "open loop" case is not presented in (c) and (d), as the powerful beam-loading effect under this condition would cause beam loss.

long-pulse, high-current conditions without feedback would cause powerful beam-loading effects resulting in beam loss.

The VOL algorithm, developed in Sec. II, was applied to this dataset to validate its performance, with results shown in Fig. 10. For the 5 μs case [Figs. 10(a) and 10(c)], the VOL-reconstructed signals from both "only CL" (red) and "CL + ILC-FF" (black) data closely match the actual "open loop" measurement (green, ground truth). For the 50 μs case [Figs. 10(b) and 10(d)], although a direct comparison with open-loop data is not available, the VOL results calculated from the "only CL" and "CL + ILC-FF" modes show excellent agreement with each other. Furthermore, in the I/Q plane [Figs. 10(c) and 10(d)], all reconstructed trajectories exhibit a straight line, which aligns with theoretical expectations. Further comparisons with BPM and BCM measurements will be provided later.

TABLE II. rf parameters for ESS buncher cavities (see Fig. 1).

| Parameter | Unit | Value |
|---|---|---|
| rf frequency | MHz | 352.21 |
| Cavity voltage | kV | 59.7 |
| Cavity half bandwidth ($\omega_{0.5}$) | kHz | ∼18 |
| Normalized shunt impedance ($r/Q$) | Ω | ∼75 |
| Coupling factor ($\beta$) | dimensionless | ∼1 |
| Beam pulse repetition rate | Hz | 14 |

Figure 11 shows the I/Q trajectories of the beam-induced rf transient for various beam currents ($I_{b0}$) and phases ($\phi_b$). These trajectories are plotted over a specific calibration time window ($T_w$), which defines the duration of the transient signal used for the analysis; for Fig. 11, $T_w = 3\,\mu s$ was used. The plots for 60 mA [Fig. 11(a)] and 5 mA [Fig. 11(b)] at various phases visually confirm that the reconstructed VOL trajectories (red crosses) accurately overlay the true open-loop response (green triangles). Figure 11(a), a representative case under the "CL + ILC-FF" control, is also included for the 60 mA, −45° beam phase (gold trajectory). The successful reconstruction in this state demonstrates the algorithm's robustness against feed-forward compensation, a feature that is systematically validated over the full current range in Fig. 15(a). Assuming the beam starts at $t_0$, the beam phase $\varphi_b$ is then determined by fitting the reconstructed trajectory $\mathbf{V}_{c,VOL}(t)$ over the window $T_w$. The final beam phase, $\varphi_b$, is given by

$$\varphi_b = 180° - \angle(\mathbf{V}_{c,VOL}(t)|_{t=t_0}^{t=t_0+T_w})_{fit}. \tag{14}$$

The statistical performance of the VOL method is quantified in Fig. 12, which plots the mean and RMS of the calibrated $\phi_b$ as a function of the calibration window $T_w$. For both the 60 mA and 5 mA cases, the mean value of the VOL method (red) [Figs. 12(a) and 12(b)] accurately

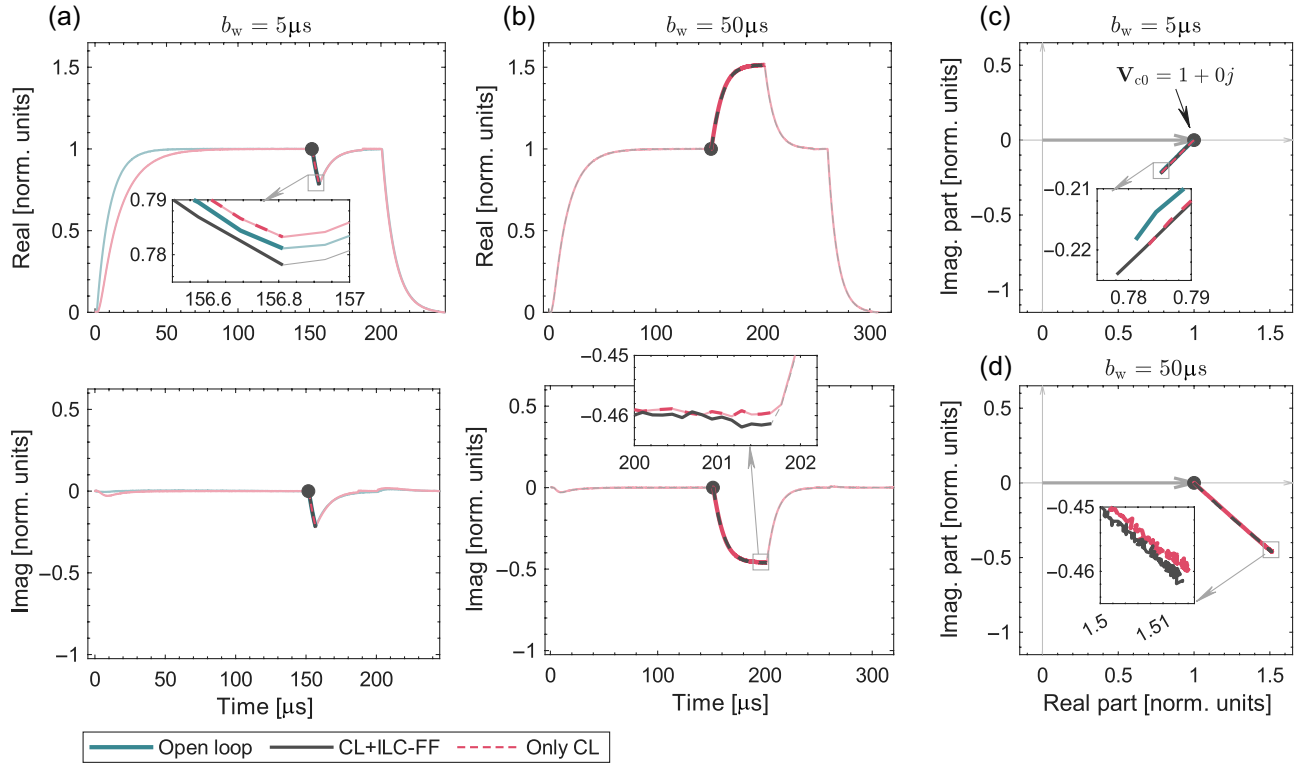



FIG. 10. Validation of the VOL algorithm using data from Fig. 9. (a),(c) 5 μs pulse; (b),(d) 50 μs pulse. The plots compare the actual "open loop" (green, ground truth) with VOL signals reconstructed from "only CL" (red) and "CL + ILC-FF" (black) data. The 50 μs "open loop" case is unavailable. The I/Q trajectories (c),(d) demonstrate that the VOL method removes control-loop effects, recovering a response approximating the true open-loop trace.

tracks the open-loop ground truth (green), independent of $T_w$. The CL method (blue), however, diverges from the true phase as $T_w$ exceeds the loop delay ($T_d \approx 1.4\,\mu s$). For the $I_{b0} = 60$ mA case [Fig. 12(a)], it is also noted that $\phi_b$ measured by both VOL and OL methods still varies by $\approx 1.5°$ as $T_w$ increases, which is related to the intrapulse phase fluctuation shown in Fig. 8(b). Observing the rms error (bottom panels), the overall measurement precision for the 60 mA case [Fig. 12(a)] is higher than for the 5 mA case [Fig. 12(b)]. This is because the larger beam current induces a stronger rf transient signal, yielding a higher signal-to-noise ratio and thus a smaller rms value. For both currents, the rms error decreases monotonically as $T_w$ increases. This improvement is attributed to the fact that a larger $T_w$ includes more data points, which enhances the statistical precision of the linear fitting used to determine the phase angle, effectively averaging out random noise.

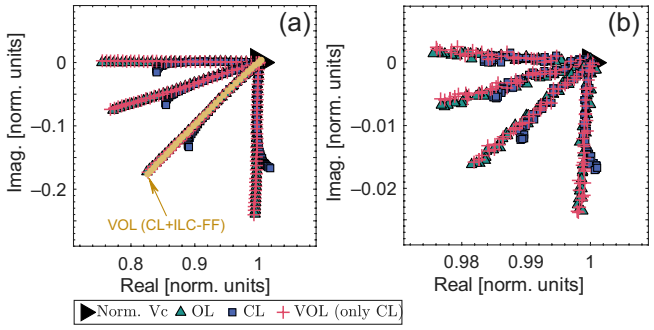



FIG. 11. I/Q trajectories for a 5 μs beam pulse ($b_w = 5\,\mu s$) at (a) 60 mA and (b) 5 mA, plotted for the first 3 μs of the transient (i.e., $T_w = 3\,\mu s$). The plots compare the actual open-loop (OL, $\mathbf{V}_{c,OL}$, green triangles), measured closed-loop (CL, $\mathbf{V}_{c,CL}$, blue squares), and reconstructed virtual open-loop (VOL, $\mathbf{V}_{c,VOL}$, red crosses) responses. The four trajectories in each subplot correspond to beam phases of approximately 1°, −18°, −44°, and −89°. The overlay of the VOL (red) and OL (green) traces confirms the algorithm's reconstruction accuracy. Additionally, a case under "CL + ILC-FF" control is included in (a) for the 60 mA, −45° beam phase (gold trajectory).

### B. Validation of the SS method

As previously demonstrated in Sec. III, a key advantage of the SS method is its robustness against cavity detuning (see Fig. 7). To build upon this finding and comprehensively evaluate the SS method's validity, we investigated its performance during a beam phase scan (60 mA, $b_w = 50\,\mu s$), with results shown in Fig. 13. During this test, the $\mathbf{V}_c$ phase was swept over ±180°, while the FB + ILC-FF system successfully held the $\mathbf{V}_c$ amplitude constant at its 60 kV setpoint [Fig. 13(a)]. The LLRF system automatically adjusted the forward voltage $\mathbf{V}_f$ to

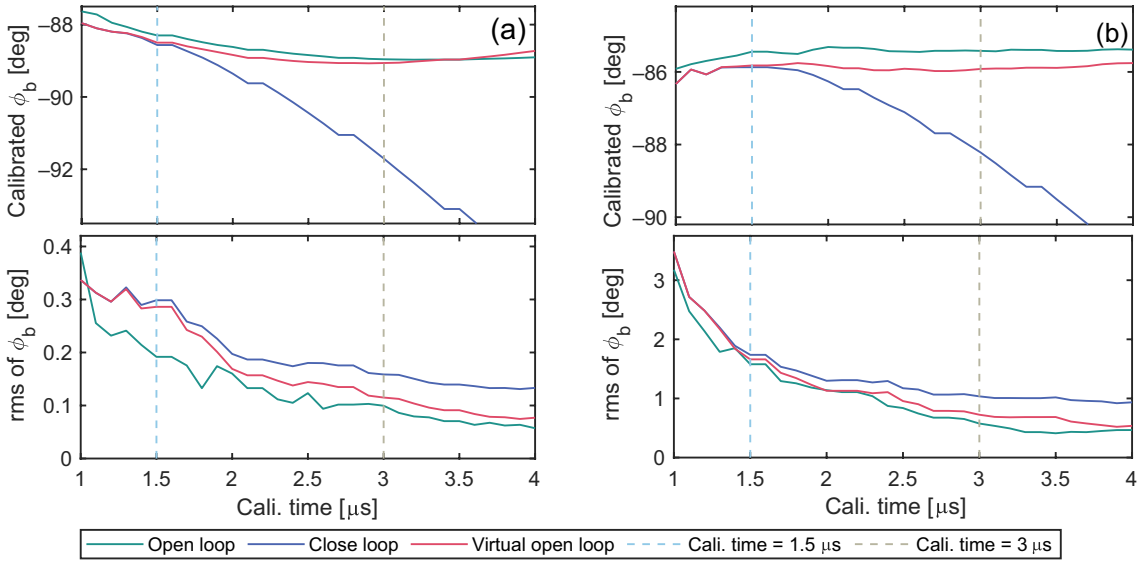



FIG. 12. Mean (top) and rms (bottom) of calibrated phase $\phi_b$ vs calibration window $T_w$, corresponding to the data in Fig. 11 for (a) 60 mA and (b) 5 mA. The VOL method (red) accurately tracks the "open loop" (green, ground truth) for all $T_w$. In contrast, the "close loop" measurement (blue) diverges for $T_w > \tau_d \approx 1.4\,\mu$s (the ESS LLRF system loop delay). The rms error (bottom panels) improves with increasing $T_w$.

compensate for the varying beam phase [Fig. 13(b)]. We then applied the SS algorithm ($\mathbf{V}_b = \mathbf{U}_p - \mathbf{U}_d$) to this dataset. The resulting phasor diagram of the calculated beam-induced voltage $\mathbf{V}_b$ [Fig. 13(c)] shows that the vector magnitude (reflecting beam current) remains nearly identical, while the phase angle correctly covers the entire scanned range. This confirms the method's accuracy across all beam phases.

Finally, we assessed the method's sensitivity to the choice of the "during beam" averaging window, a practical consideration for implementation. As shown in Fig. 14(a), the steady-state drive $\mathbf{U}_d$ was averaged over five distinct 10 μs windows (e.g., $W_1$: 162–172 μs, green; $W_4$: 180–190 μs, black; $W_5$: 186–196 μs, blue) within the stable flattop. The top panel of Fig. 14(b) plots the "phase offset" (defined as the measured beam phase $\phi_b$ relative to the rf

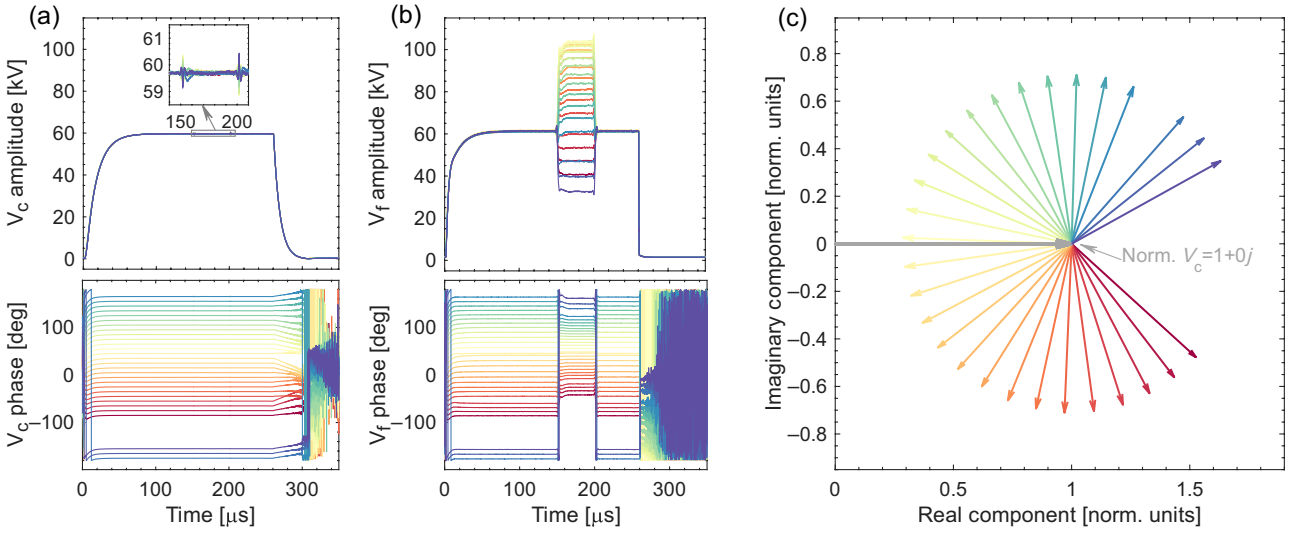



FIG. 13. Demonstration of the SS method during a beam phase scan (60 mA, $b_w = 50\,\mu$s). (a) The cavity voltage ($\mathbf{V}_c$) amplitude (top) is held constant at its setpoint (e.g., 60 kV) by the FB + ILC-FF control system, while its phase (bottom) is swept between ±180°. (b) The corresponding forward voltage ($\mathbf{V}_f$) (amplitude and phase) provided by the LLRF system to compensate for the varying beam phase. (c) Phasor diagram of the beam-induced voltage ($\mathbf{V}_b$) calculated using the SS method ($\mathbf{V}_b = \mathbf{U}_p - \mathbf{U}_d$). The magnitudes of all colored vectors (reflecting beam current) are nearly identical, while their phase angles cover the entire scan range. The visible gap in the decelerating regime is attributed to a machine interlock that occurred during the phase scan, which interrupted data acquisition for those specific phases.

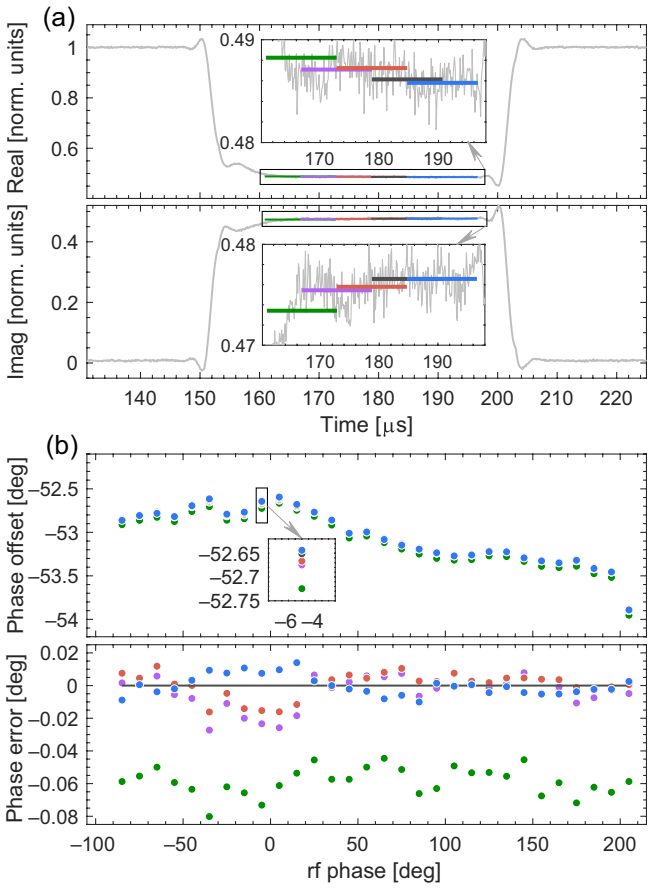



FIG. 14. Sensitivity of the SS method to the "during beam" averaging window used to calculate $\mathbf{U_d}$. (a) The drive $\mathbf{U_d}$ is averaged over five distinct 10 μs windows (e.g., $W_1$: 162–172 μs; $W_4$: 180–190 μs; $W_5$: 186–196 μs) within the stable flattop. (b) Top: "phase offset" ($\phi_b - \phi_{\mathrm{RF,set}}$) vs scanned rf phase for all five windows. Bottom: "phase error," showing the deviation of each window relative to the $W_4$ (180–190 μs) reference. The near-perfect overlay (top) demonstrates the method's robustness, showing it is insensitive to the specific choice of the averaging window within the flattop.

setpoint phase $\phi_{\mathrm{rf,set}}$) vs the scanned rf phase for all five windows. The bottom panel plots the "phase error," showing the deviation of each window's offset relative to the $W_4$ (180–190 μs) reference window. The near-perfect overlay in the top panel demonstrates that the SS method is robust and insensitive to the specific choice of the averaging window, provided it is within the stable flattop region.

It is worth noting that during the phase scan process in Fig. 13, the cavity detuning also varies. This detuning variation can be directly observed from the change in the slope of the phase curve after the rf is turned off in Fig. 13(a) (bottom). The fact that the calculated "phase offset" in Fig. 14(b) remains approximately stable under these conditions further confirms the robustness of the SS method itself against detuning. This point is further illustrated in the subsequent Fig. 18.

### C. Comparison with beam diagnostics

To confirm the absolute accuracy of the proposed methods, the rf-based measurements were benchmarked against independent beam diagnostics (BPM/BCT). The statistical uncertainty of the BPM-derived phase is approximately 0.15°. Figure 15 presents this validation for the $b_w = 5$ μs beam pulse case. It is critical to note that for this short pulse, the forward voltage $\mathbf{V_f}$ does not reach a steady state during the beam pulse, as is evident in Fig. 9(b). Therefore, the prerequisite for the SS method is not met.

Figure 15(a) shows the results for buncher 1 (using BPM2), which operated with the FB + ILC-FF control loop fully engaged. In this mode, the CL method is not applicable. The ILC-FF provides compensation that is already active within the $T_{\mathrm{d}}$ window, violating the method's assumption of a control-free interval. Thus, the plot compares only the applicable VOL method (red) with the BPM2 reference (green), showing excellent agreement across the entire current range.

Figures 15(b) and 15(c) show results for buncher 2 (using BPM3), which operated with only the FB loop active ("only CL"). This allows a direct comparison between the VOL method (red) and the CL method (blue) against the BPM3 reference (green). Again, the VOL results accurately track the BPM reference. The CL method measurement, however, clearly diverges from the BPM reference as the beam current increases [19]. This increasing deviation at higher currents is attributed to the intrapulse beam phase fluctuations [seen in Fig. 8(d)], which can introduce an error of approximately 1.5° in the closed-loop fit. It is also noted that the BPM reference itself varies with current; this may be attributed to defocusing effects within the buncher cavity, which can cause beams of different intensities to follow slightly different orbits and thus register differently on the BPM. The VOL method successfully tracks all these variations, confirming its accuracy and robustness.

We then performed a direct comparison of the VOL and SS methods under conditions where both are applicable. This test used a long beam pulse ($b_w = 50$ μs) with the FB + ILC-FF control loop engaged. The 50 50 μs pulse ensures that the forward voltage reaches a stable plateau [as seen in Fig. 9(d)], satisfying the prerequisite for the SS method.

The comparative results are benchmarked against the BPM reference (with a statistical uncertainty of 0.15°) in Fig. 16. Figures 16(a) and 16(c) show the results for buncher 1, while Figs. 16(b) and 16(d) show the results for buncher 2. Figures 16(a) and 16(b) present the statistical distributions (histograms) from 120 measurements at each of 10 different current steps (from 3.0 to 64.2 mA). The corresponding mean values are plotted against beam

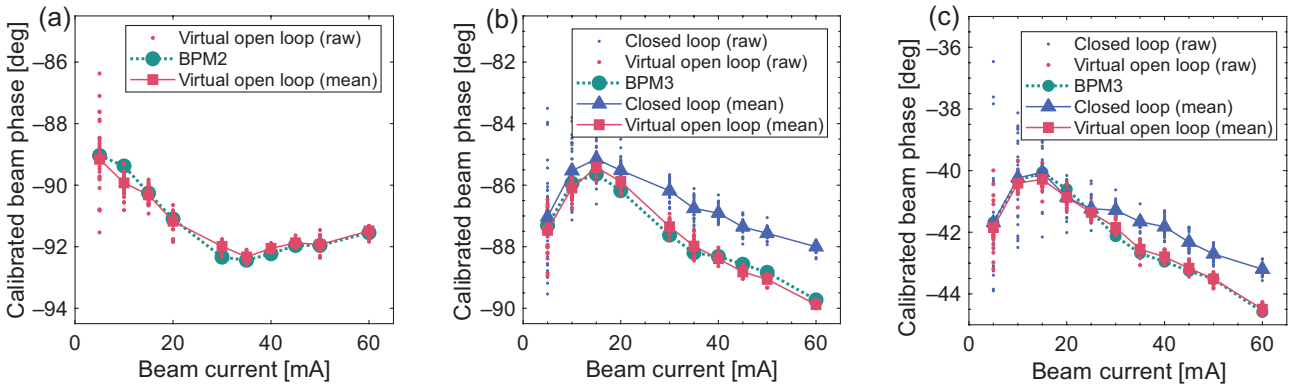



FIG. 15. Comparison of calibrated beam phase vs beam current under different LLRF control configurations, validated against independent BPM diagnostics (statistical uncertainty ≈0.15°). (a) Results for buncher 1 under combined feedback and iterative learning control (FB + ILC-FF) operation, comparing the VOL method (red squares) with the BPM2 reference (green circles). (b),(c) Results for buncher 2 under feedback-only (FB) control, comparing the VOL method (red squares) and CL method (blue triangles) with the BPM3 reference. The VOL method maintains excellent agreement with the BPM references across both configurations. In contrast, the standard CL measurements in (b),(c) diverge from the reference as the beam current increases. Small dots represent the corresponding raw, single-shot data.

current in Figs. 16(c) and 16(d). The results show that both the VOL (red) and SS (black) methods maintain excellent agreement with the BPM reference (green) across the tested current range. The bimodal distributions in some histograms are primarily caused by the dynamic adjustment of the ILC algorithm. Typically, the ILC requires more than ten pulses to update the feed-forward tables. The algorithm deactivates when the error falls below a predefined threshold and retriggers if the error exceeds it. This process induces transient oscillations within the measurement window, leading to a bimodal probability density in certain cases.

In addition to phase calibration, we also evaluated the beam current calibration accuracy of the VOL and SS methods using buncher 2 as an example, with the results benchmarked against a BCT (in front of B2, see Fig. 1) in Fig. 17. Panel (a) plots the calibrated current from both methods ($I_{\mathrm{b0,cali}}$) against the BCM ground-truth measurement ($I_{\mathrm{b0,BCT}}$). Panel (b) shows the relative error, $E_{\mathrm{relative}}$, which is calculated as

$$E_{\mathrm{relative}} = \frac{I_{\mathrm{b0,cali}} - I_{\mathrm{b0,BCT}}}{I_{\mathrm{b0,BCT}}} \times 100\% \tag{15}$$

where $I_{\mathrm{b0,cali}}$ represents the current calibrated by the rf methods (VOL or SS) and $I_{\mathrm{b0,BCM}}$ is the reference current from the BCT. As shown in Fig. 17(b), both the VOL and SS (black) methods exhibit a larger error at low beam currents, with the SS method even exceeding 5%. This is likely related to the weaker beam-loading strength at low current. Overall, for $I_{\mathrm{b0}} > 20$ mA, the measurement error for both methods is within ±4%.

As previously established (Sec. II), the accuracy of the VOL method is contingent upon cavity detuning, whereas the SS method (Sec. III) is inherently robust to this effect. We observed that during a one-hour phase-scan, the cavity detuning varied, which in turn impacted the uncalibrated VOL measurement results. Figure 18(a) shows the rf phase setpoint ($\phi_{\mathrm{rf,set}}$) being swept over time, alongside the resulting beam phase measurements from the VOL (red) and SS (blue) methods. The measured $\Delta f$ (green) is shown in Fig. 18(b) (top), which was simultaneously drifting. The critical finding is in Fig. 18(b) (bottom), which plots the "phase offset" ($\phi_b - \phi_{\mathrm{RF,set}}$) calculated by the algorithms. The uncalibrated VOL (blue) trace is clearly correlated with the detuning drift, whereas the SS (black) and calibrated VOL (red) traces remain stable. This dependence is explicitly confirmed in Fig. 18(c), which plots the "phase offset" directly against $\Delta f$, revealing the strong linear correlation of the uncalibrated VOL method. A detailed discussion on how detuning impacts phase measurements in NC cavities and the corresponding calibration procedure is available in Ref. [19].

The final result is shown in Fig. 18(f), plotting the "phase offset" against the scanned rf phase. It demonstrates that after detuning calibration is applied, the VOL method (red) successfully compensates for the $\Delta f$ drift and aligns perfectly with the SS method (blue). Both methods remain stable and exhibit good agreement, with a maximum error within ±0.5°.

Since both the VOL and SS methods require the calibrated forward signal, we also evaluated the distribution of the normalized calibration coefficients $X$ and $Y$. The insets (d), (e) show their distributions, indicating that the coefficients exhibit a variation range of approximately ±0.3%. In practice, we use the average of 120 pulses for $X$ to calculate the actual $\mathbf{V}_{\mathrm{f}}$ signal.

Taken together, the ESS buncher measurements demonstrate that both the VOL and SS schemes can deliver accurate online beam-phase and current calibration under

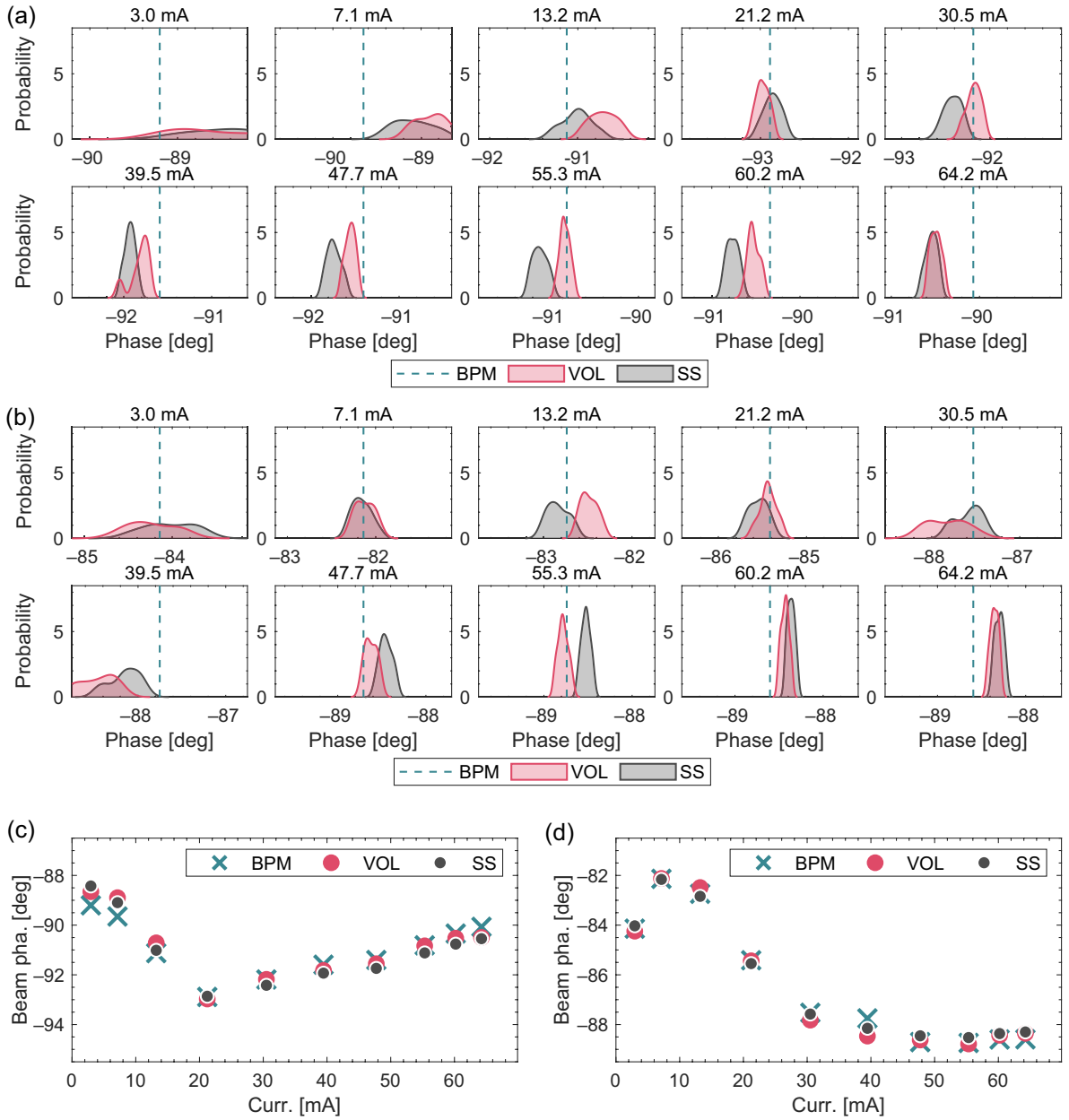



FIG. 16. Direct comparison of the VOL and SS methods against the BPM ground truth (statistical uncertainty ≈0.15°) under long-pulse ($b_w = 50\,\mu s$) and FB + ILC-FF operation. (a),(c) show the results for buncher 1; (b),(d) show the results for buncher 2. (a),(b) Histograms of the measured phase from all three methods (BPM: green, VOL: red, SS: black) for 10 different beam current levels. (c) and (d) Corresponding mean calibrated phase plotted against beam current.

closed-loop operation, with performance consistent with independent BPM/BCT diagnostics. These experimentally validated results provide the basis for the comparative discussion and application guidelines in Sec. V.

## V. COMPARISON AND DISCUSSION

The experimental validation in Sec. IV confirms that both the VOL and SS methods provide accurate, real-time beam parameter estimates under closed-loop conditions, in good agreement with independent diagnostics. Their respective strengths and limitations determine their optimal domains of application.

### A. Comparative analysis and application guidelines

The CL method, which fits the transient within the loop delay window, is conceptually simple because it effectively performs an "instantaneous" open-loop measurement for $t < T_d$ [10,11,13,18]. However, this simplicity also defines its main drawback: the finite number of samples available within $T_d$ (e.g., $\approx 1.4\,\mu s$ at ESS)

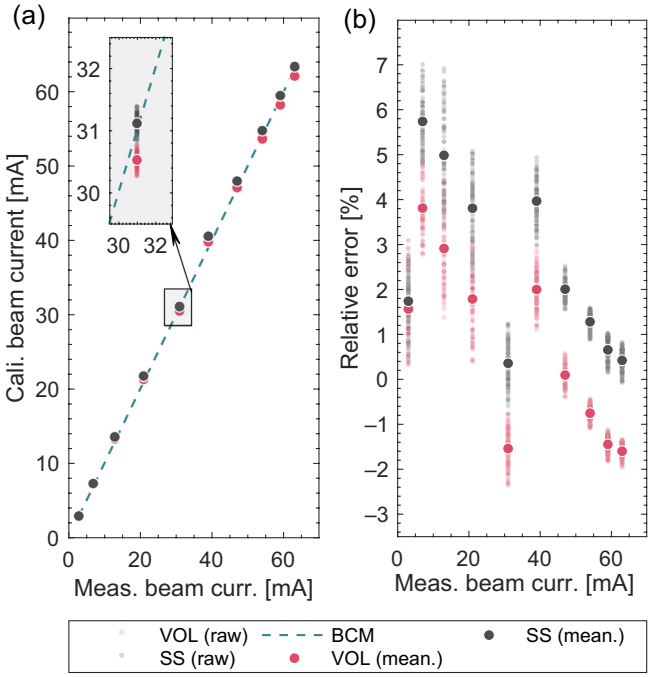



FIG. 17. Beam current calibration accuracy for the VOL (red) and SS (black) methods on buncher 2, benchmarked against the BCM (blue, ground truth). These data correspond to the 50 μs pulse with FB + ILC-FF control. (a) Calibrated current from both methods vs the BCT measurement. (b) Relative error of the VOL and SS methods with respect to the BCT. The results show that the SS method (black) has a larger error (exceeding 5%) at low beam currents. Overall, the measurement error for both methods is within ±4%.

fundamentally limits the achievable resolution. This is experimentally confirmed in Figs. 15(b) and 15(c), where the CL method (blue triangles) deviates from the BPM reference by up to ≈2° at high beam currents [19].

The VOL method is highly flexible, requiring no assumptions about the steady-state condition of either $\mathbf{V}_c$ or $\mathbf{V}_f$. It can therefore be applied to short and long pulses, with or without feedforward, as demonstrated by the 5 μs validation in Figs. 9 and 10, where a steady state was never reached. Its main limitation is the sensitivity to cavity detuning. As the calibration window $T_w$ increases, the uncalibrated VOL phase measurement exhibits a strong correlation with $\Delta f$, as shown in Figs. 18(b) and 18(c), and thus requires an explicit detuning calibration [19,22,24]. Once this correction is applied, the VOL results are stable and agree well with both BPM and SS measurements, with a residual phase error within ±0.5° [Fig. 18(f)].

In contrast, the SS method is intrinsically robust against cavity detuning. As long as the LLRF system maintains a constant cavity field during the flattop, the beam-induced voltage is directly obtained from the vector difference of the steady-state forward drive phasors, $\mathbf{V}_b = \mathbf{U}_p - \mathbf{U}_d$, and is essentially insensitive to $\Delta f$ (Figs. 7 and 14). This robustness is further confirmed in Fig. 18, where the SS phase offset remains stable despite significant detuning drift. The price for this advantage is a stricter prerequisite: both $\mathbf{V}_c$ and $\mathbf{V}_f$ must have reached a stable, steady state. As a result, the SS method is not applicable to very short pulses or to loops that do not fully compensate for beam loading. In practice, it is best suited to long-pulse operation with effective FB + FF (e.g., FB + ILC-FF) control and a well-defined rf flattop.

Finally, both VOL and SS methods depend critically on the accurate calibration of the raw LLRF signals ($\mathbf{V}_f^*$, $\mathbf{V}_r^*$) used to reconstruct the physical cavity and forward voltages via Eq. (2). Using multiple pulses to average the calibration coefficients $X$ and $Y$ is a recommended strategy. Furthermore, for some scenarios (e.g., limited directivity of directional couplers, or crosstalk between ADC channels and/or cavities), a more precise crosstalk calibration algorithm may be needed to achieve high-accuracy rf signal calibration [20]. In addition to signal calibration, the accuracy of cavity parameters is also critical. For the VOL method, which requires solving the cavity difference equation [Eq. (6)], the accurate measurement of parameters such as $\omega_{0.5}$ and $\Delta\omega$ is essential. The SS method also requires accurate cavity parameters when calculating the beam current via Eq. (12), for example $(r/Q)$ and $Q_L$ [28,29]. Further improvements in both signal calibration stability and parameter identification would directly translate into even more accurate and robust online beam phase and current measurements in routine operation. To provide a clear overview of the operational tradeoffs and performance characteristics discussed above, the properties of the Td-based, SS, and VOL methods are summarized in Table III.

### B. Systematic uncertainty analysis

To evaluate the proposed framework, we perform a systematic uncertainty analysis focusing on the SS method as a representative case study. Its direct dependence on steady-state signals allows for a clear decomposition of error contributions. Regarding the VOL method, the numerical solution of differential equations involves more indirect and intricate error propagation pathways; a detailed expansion of its uncertainty is thus beyond the scope of the present study.

According to Eq. (12), $I_{b0}$ and $\varphi_b$ are synthesized from the reconstructed voltage $\mathbf{V}_b$, which is determined by the forward signals $\mathbf{U}_p$ and $\mathbf{U}_d$. Based on the distributions in Fig. 18(d), the relative amplitude and phase uncertainties of the calibration coefficient $X$ are $\delta_{|X|} \approx 0.15\%$ and $\Delta\angle X \approx 0.17°$, respectively.

#### 1. Phase uncertainty

The uncertainty of $\varphi_b$ is dominated by the phase error of $X$ (0.17°), which transfers linearly to the measurement. Accounting for an additional 0.07° uncertainty from

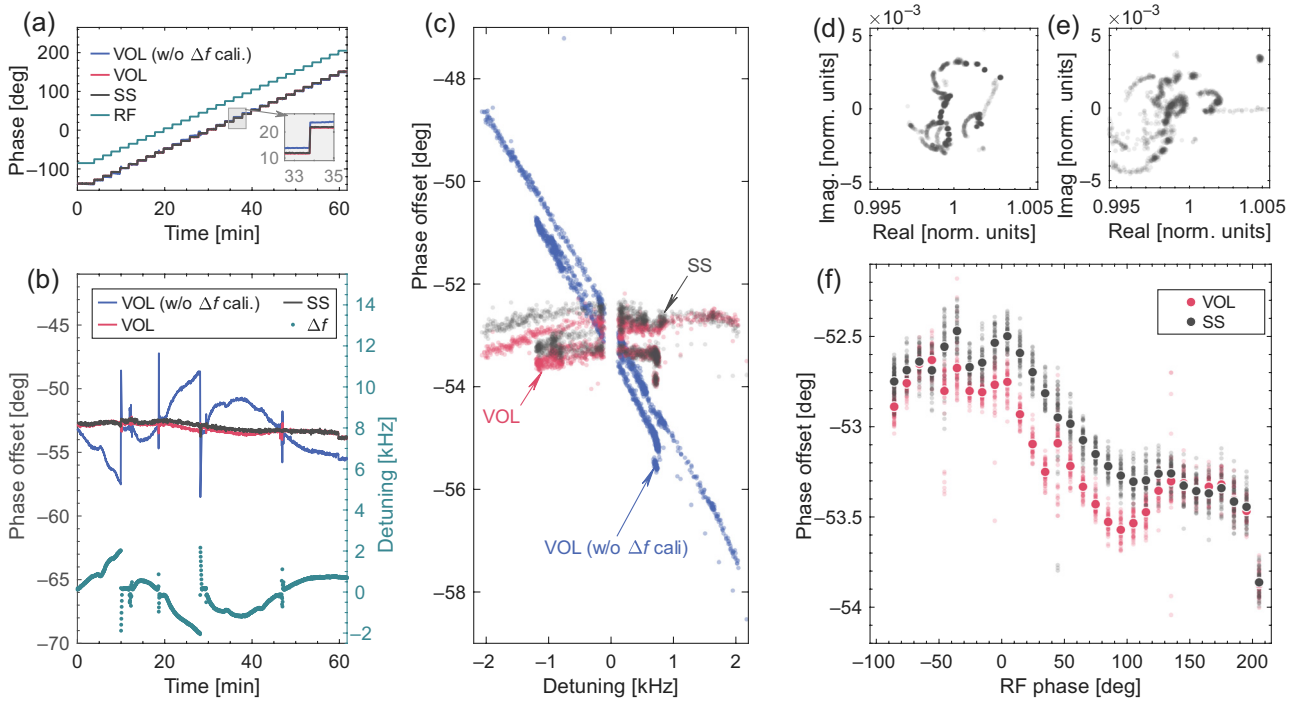



FIG. 18. Comparison of VOL and SS methods during a 60 mA, $b_w = 50\,\mu$s beam phase scan with accompanying detuning variation. (a) The rf phase setpoint ($\phi_{\mathrm{rf,set}}$) swept over time, and the beam phase measured by the VOL (red) and SS (blue) methods. (b) Measured cavity detuning ($\Delta f$) (green), and the "phase offset" ($\phi_b - \phi_{\mathrm{rf,set}}$) over time for SS (black), VOL (calibrated, red), and VOL (uncalibrated, blue). (c) Direct correlation of "phase offset" vs detuning, showing the uncalibrated VOL method's strong dependence on $\Delta f$. (f) Final "phase offset" vs the scanned rf phase, showing the calibrated VOL (red) and SS (blue) methods exhibit good agreement, with a maximum error within $\pm 0.5°$. Subplots (d),(e) show the normalized distributions of calibration coefficients $X$ and $Y$ during the measurement.

the window-averaging process, the combined systematic phase uncertainty is evaluated as $\sqrt{0.17^2 + 0.07^2} \approx 0.18°$. This theoretical estimate is highly consistent with the experimentally observed average deviation of $\approx 0.2°$ relative to BPM data.

### 2. Current uncertainty.

The uncertainty of $I_{\mathrm{b0}}$ is inherently more pronounced than that of the phase because, as defined by Eq. (12); it is synthesized from several independent physical parameters. To evaluate the combined error, we define $\delta_x = \Delta x/x$ as the relative systematic uncertainty of parameter $x$. Based on the error propagation framework, the total relative uncertainty is given by

$$\delta_{I_{\mathrm{b0}}} = \sqrt{\delta^2_{|V_{\mathrm{b}}|} + \delta^2_G + \delta^2_{r/Q} + \delta^2_{Q_{\mathrm{L}}}}. \tag{16}$$

The voltage $\delta_{|V_{\mathrm{b}}|}$ inherits the 0.15% LLRF signal precision evaluated from the calibration coefficient $X$ distribution. The gain $G$, mapping normalized cavity

TABLE III. Comparison of three nonintrusive online beam calibration methods.

| Feature | $T_d$-based CL | Steady-state (SS) | Virtual open-loop (VOL) |
|---|---|---|---|
| Beam pulse | Arbitrary | Long pulse (flat-top) | Arbitrary |
| rf control mode | Feedback only | Typically FB + FF | No special requirement |
| System state requirement | No special requirement | $V_f$ and detuning in steady state | No special requirement |
| Detuning calibration requirement | Generally not required[a] | Not required | Required |
| Signal calibration | Not required | Required | Required |
| $V_c$ accuracy requirement | Low | High | Low |
| Accuracy and precision | Generally lower | High (depends on calibration level) | High (comparable to SS) |

[a]Depends on the loop delay and detuning. In cases where the loop delay is much smaller than the cavity time constant $\tau$ and the detuning is less than the cavity half-bandwidth, calibration is generally not required; see Ref. [19] for details.

voltage to physical values, is typically calibrated via beam-based energy gain measurements; while such calibrations in the low-energy region range from 1% to 2%, we adopt a conservative maximum of $\delta_G = 2\%$ [30,32]. Furthermore, the geometric parameter $r/Q$ is determined via 3D electromagnetic simulations, which may exhibit a discrepancy of $\delta_{r/Q} \approx 3\%$ from true physical values due to fabrication tolerances [31]. Finally, $Q_{\mathrm{L}}$ is conventionally obtained from rf field decay measurements and is susceptible to finite coupler directivity and RF source-end reflections [28,29]. Given that the ESS MEBT is equipped with high-power circulators and directional couplers exceeding 40 dB directivity, a practical uncertainty of $\delta_{Q_{\mathrm{L}}} \approx 2\%$ is assumed. Substituting these values yields the combined systematic uncertainty for the current measurement:

$$\frac{\Delta I_{\mathrm{b0}}}{I_{\mathrm{b0}}} = \sqrt{(0.15\%)^2 + (2\%)^2 + (3\%)^2 + (2\%)^2} \approx 4.1\%. \tag{17}$$

It should be noted that the synthesis above provides a simplified, first-order estimation of the systematic uncertainty based on conservative assumptions of parameter tolerances. While the actual error environment in operation is undoubtedly more complex, the fact that the estimated ≈4.1% aligns in magnitude with the experimental deviations shown in Fig. 17(b) serves as a reasonable validation of the error budget. This framework explains the fundamental precision gap between the two measurements: beam phase precision is primarily constrained by a single dominant factor (LLRF phase calibration), whereas current estimation inherently suffers from the cumulative uncertainty of a much broader stack of independent physical parameters.

## VI. CONCLUSION AND OUTLOOK

Accurate online calibration of beam parameters is essential for high-power linacs, yet established methods face significant limitations. The OL method, while effective, is unsuitable for high-current proton accelerators because of the unacceptable risk of beam loss and trips. Safer CL methods based on the loop-delay window $T_{\mathrm{d}}$ avoid these risks, but the available analysis window (e.g., ≈1.4 μs at ESS) is too brief to provide sufficient sampling. This fundamentally limits the attainable measurement precision and leads to significant deviations (up to ≈2°) at high beam currents, as confirmed in this work (Fig. 15).

To overcome these precision and safety limitations, this paper has developed and experimentally validated two complementary schemes: the VOL and the SS methods. The VOL method reconstructs an equivalent open-loop beam-induced response by numerically removing control-loop effects. The SS method infers the beam phasor from the steady-state vector difference of the forward drive signals. Both approaches were systematically demonstrated on an ESS NCRF buncher cavity, achieving excellent agreement with independent BPM/BCT diagnostics, with a phase accuracy better than ±0.5° and a current accuracy within ±4% for $I_{b0} \gtrsim 20$ mA.

These results confirm that the two methods have distinct yet complementary domains of application. The VOL method is highly flexible and can be applied even to short pulses (5 μs) where a steady state is not reached (Figs. 9 and 10). Its main drawback is its sensitivity to cavity detuning, which necessitates an explicit detuning calibration for normal-conducting rf cavities. Conversely, the SS method's key advantage is its intrinsic robustness to detuning. This robustness, however, relies on a stricter prerequisite: the LLRF system must establish a stable steady state, limiting its applicability to long pulses with effective FB + FF compensation. For superconducting cavities, the large filling time constant may partly relax the detuning-calibration requirement for the VOL method. However, the dynamic LFD inherent to pulsed SRF operation necessitates a time-varying generalization of the VOL algorithm. The detailed mathematical framework for this time-varying generalization, along with a preliminary experimental validation demonstrating its effectiveness on multiple SRF cavities at the HIAF facility, is comprehensively presented in the Appendix.

While the present experimental validation was conducted on single-cell cavities, extending these methods to multicell structures requires considering the excitation of nearby parasitic passband modes (e.g., the $8\pi/9$ mode for a nine-cell cavity). Although these modes could perturb the reconstructed fundamental-mode voltage, their impacts can likely be mitigated, as the sharp digital low-pass filters (or notch filters) in modern LLRF systems heavily attenuate these modes. Indeed, the effectiveness of the SS method for such complex structures has been initially validated on the multicell RFQ at the ESS [33], where it was employed to monitor beam phase and energy gain during high-power operation. Further quantitative experimental verifications of these effects across various multicell cavity types are planned for future investigations.

Looking ahead, the VOL and SS schemes provide a nonintrusive and broadly applicable toolkit for real-time beam monitoring during high-power operation. Integrating these techniques with routine LLRF diagnostics, automated calibration procedures, and fast cavity-parameter identification is a promising path toward fully online, high-precision beam phase and current monitoring in next-generation high-intensity linacs.

## ACKNOWLEDGMENTS

This work was supported by the studies of intelligent LLRF control algorithms for superconducting RF cavities (Grant No. E129851YR0). We would like to thank all

members of the European Spallation Source (ESS) commissioning team for providing the stable beam operation.

## APPENDIX: GENERALIZATION OF THE VOL METHOD FOR SRF CAVITIES WITH DYNAMIC DETUNING

The derivation of the VOL method in Sec. II assumes a constant $\Delta\omega$, which is a reasonable approximation for normal-conducting cavities due to their high mechanical stiffness. However, SRF cavities, characterized by large time constants and pulsed operation at high gradients, exhibit significant dynamic LFD, denoted as $\Delta\omega(t)$. To accurately reconstruct beam-induced transients under such conditions, the constant-parameter discrete difference equation must be generalized to incorporate these time-dependent dynamics. To accommodate dynamic detuning, the differential equation governing the cavity voltage is extended to a linear time-varying (LTV) system. By representing the signals as complex vectors $\mathbf{V}_c$ and $\mathbf{U}$, the generalized equation is expressed as

$$\frac{d\mathbf{V}_c}{dt} + [\omega_{0.5} - j\Delta\omega(t)]\mathbf{V}_c = \underbrace{\omega_{0.5}\mathbf{U}}_{\text{loop drive}} + \underbrace{\omega_{0.5}\mathbf{V}_b}_{\text{beam loading}}, \quad \text{(A1)}$$

where $\mathbf{U} = \frac{2\beta}{1+\beta}\mathbf{V}_f$ represents the equivalent forward drive signal fed by the control loop. Because the superposition principle rigorously holds for LTV systems, the loop-driven response $\mathbf{V}_{cf}$, excited solely by the forward drive $\mathbf{U}$, can be decoupled as

$$\frac{d\mathbf{V}_{cf}}{dt} + [\omega_{0.5} - j\Delta\omega(t)]\mathbf{V}_{cf} = \omega_{0.5}\mathbf{U}. \quad \text{(A2)}$$

The corresponding state-space difference equation is obtained as

$$\begin{bmatrix} V_{cf,i}(n+1) \\ V_{cf,q}(n+1) \end{bmatrix} = \begin{bmatrix} 1 - T_s\omega_{0.5} & -T_s\Delta\omega(n) \\ T_s\Delta\omega(n) & 1 - T_s\omega_{0.5} \end{bmatrix} \begin{bmatrix} V_{cf,i}(n) \\ V_{cf,q}(n) \end{bmatrix} + T_s\omega_{0.5} \begin{bmatrix} U_i(n) \\ U_q(n) \end{bmatrix}. \quad \text{(A3)}$$

Here, $V_{cf,i}(n)$ and $V_{cf,q}(n)$ denote the I/Q components of the loop-driven response $\mathbf{V}_{cf}$ at step $n$. Similarly, $U_i(n)$ and $U_q(n)$ correspond to the I/Q components of the forward drive $\boldsymbol{U}$. $T_s$ is the sampling interval, and $\Delta\omega(n)$ is the sampled dynamic detuning.

The applicability of the generalized method was experimentally validated using an SRF cavity at the High Intensity Heavy-ion Accelerator Facility (HIAF) [34–36]. As illustrated in Fig. 19, a weak beam pulse (approx. 200 eμA, 900 μs) was injected at $t = 7.8$ ms. The resulting beam-loading effect was minimal, inducing perturbations of only ±0.2% in amplitude and ±0.2° in phase under FB-only control. In the absence of active fast tuners, the dynamic LFD remains uncompensated, causing the cavity detuning and the required $\mathbf{V}_f$ to vary continuously throughout the rf flattop (5 to 19.8 ms).

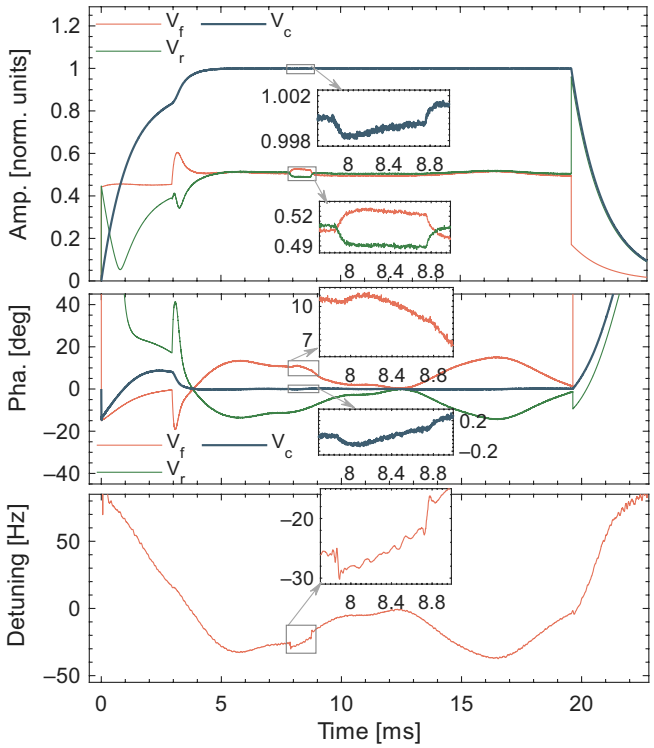



FIG. 19. Measured rf waveforms and time-varying cavity parameters for the HIAF SRF cavity. The data capture the signal waveforms during the injection of a weak beam pulse (200 μA, 900 μs) under feedback-only control. Top to bottom: amplitudes (top) and phases (middle) of the cavity, forward, and reflected voltages, and the dynamic cavity detuning (bottom). Note that because the beam-loading term is not subtracted in the conventional detuning calculation algorithm, the measured dynamic detuning is slightly perturbed during the beam passage (visible as a small dip in the curve).

In the absence of the beam, the dynamic detuning can be conventionally calculated using the fundamental cavity phase equation:

$$\Delta\omega = \frac{d\phi}{dt} - \frac{\omega_{0.5}|2\mathbf{V}_f|\sin(\theta - \phi)}{|\mathbf{V}_c|}, \quad \text{(A4)}$$

where $|\mathbf{V}_c|$ and $|\mathbf{V}_f|$ are the amplitudes of the cavity and forward voltages, respectively, while $\phi$ and $\theta$ denote their corresponding phases. $\omega_{0.5}$ is the cavity half-bandwidth.

However, because Eq. (A4) neglects the beam-loading term, its application during beam passage yields a distorted result. As shown in Figs. 19 and 20(a), this uncompensated effect manifests as a numerical dip in the calculated detuning, masking the true trajectory. Physically, because the cavity field amplitude is stabilized by the feedback loop, the resulting Lorentz force remains continuous.

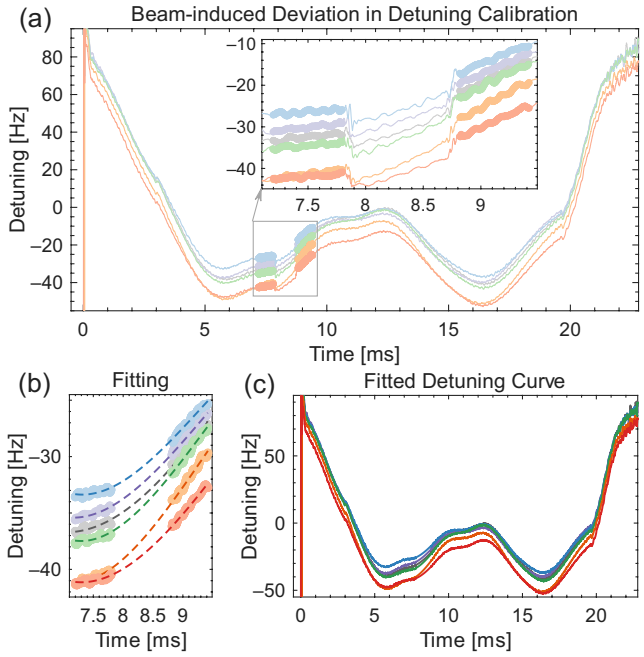



FIG. 20. Fitting and correction of the dynamic detuning during the beam pulse. (a) Computation deviation (visible as a dip) in the measured detuning during the beam passage (7.8–8.7 ms), caused by the uncompensated beam-loading effect. (b) Polynomial fitting (dashed lines) using valid detuning data points (solid dots) sampled before and after the beam to interpolate the true detuning. (c) The corrected, smooth dynamic detuning curves across the entire rf flattop, which are used for the subsequent time-varying VOL algorithm.

Consequently, the true dynamic detuning must be intrinsically smooth. To address this, we extract valid detuning data immediately before and after the beam pulse and apply a polynomial fit to interpolate the trajectory across the beam window [Fig. 20(b)]. This correction, shown in [Fig. 20(c)], provides the $\Delta\omega(n)$ sequence required for Eq. (A3).

With the reconstructed dynamic detuning, the time-varying VOL algorithm is executed using Eq. (A3). As shown in Fig. 21(a), while the feedback regulation on the measured cavity field $\mathbf{V}_c$ hides the microscopic beam-loading signature, the iterative calculation and subtraction of the loop-driven response $\mathbf{V}_{cf}$ successfully isolates the beam-induced transient $\mathbf{V}_{c,VOL}$. Projecting this transient onto the $I/Q$ plane reveals a distinct linear trajectory [Fig. 21(b)], from which the beam phase is extracted via a linear fit. Notably, an average detuning of approximately $-26$ Hz during the beam passage (see Fig. 19) causes a clockwise deflection of this trajectory. The resulting estimation biases in phase and amplitude can be analytically calibrated using the method detailed in Ref. [19].

Statistical beam tests were performed across ten quarter-wave resonators (QWR007-type) located in the first (CM1) and sixth (CM6) cryomodules of the HIAF iLinac [37]. These specific modules were operated in pulsed mode to facilitate the necessary forward signal calibration. At its current commissioning stage, HIAF operates with beam currents in the hundreds of microamperes, presenting significantly weaker signals than

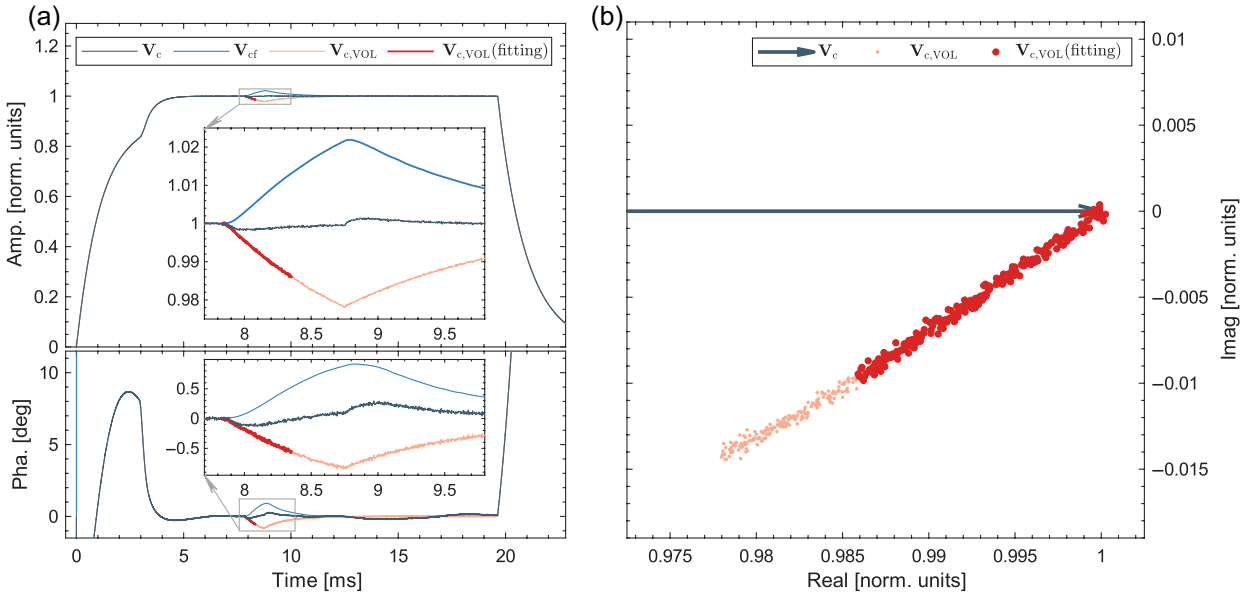



FIG. 21. Demonstration of the time-varying VOL algorithm applied to the HIAF SRF cavity under non-steady-state conditions. (a) Time-domain amplitudes (top) and phases (bottom) of the measured cavity field ($\mathbf{V}_c$), the calculated loop-driven response ($\mathbf{V}_{cf}$), and the reconstructed pure beam-induced transient ($\mathbf{V}_{c,VOL}$). (b) Corresponding signal trajectories in the $I/Q$ plane. A linear fit to this trajectory yields the beam phase, where the dark red dots represent the reconstructed trajectory during the initial 500 μs. This specific window is selected to minimize the impact of cumulative time-varying detuning and ensure high-fidelity phase extraction under weak beam loading conditions.

TABLE IV. Comparison of lattice and measured phases for HIAF cavities in CM1 and CM6 cryomodules.

| Cavity No. | Lattice (deg) | Meas. (deg) | Err (deg) |
|---|---|---|---|
| CM1-1 | −40 | −40.5 | −0.5° |
| CM1-2 | −39 | −37.6 | 1.4° |
| CM1-3 | −38 | −36.1 | 1.9° |
| CM1-4 | −40 | −40.8 | −0.8° |
| CM1-5 | −34 | −34.4 | −0.4° |
| CM6-1 | −37 | −39.1 | −2.1° |
| CM6-2 | −26 | −27.4 | −1.4° |
| CM6-3 | −25 | −26.4 | −1.4° |
| CM6-4 | −42 | −40.2 | 1.8° |
| CM6-5 | −30 | −28.3 | 1.7° |

those at high-current facilities such as the ESS. Table IV summarizes the comparison between the measured beam phases and the theoretical lattice design values.

The experimental results demonstrate a mean absolute error of 1.3° across all tested cavities, with the maximum absolute error being approximately 2°. While this margin is wider than that achieved at ESS, it is primarily due to the exceptionally low beam-loading ratio during the initial HIAF commissioning. Specifically, with a 200 eμA beam current against a 25 MV/m peak gradient field (whereas the final design current is on the order of several mA), the beam-induced rf transient accounts for only approximately 0.2% of the total gradient under closed-loop control. Despite these challenging signal-to-noise conditions, the precision provides an independent reference for verifying the physical lattice and identifying potential fault sources. Measurement accuracy is expected to improve linearly as the beam current scales up in future operations. These tests successfully confirm the feasibility and robustness of the time-varying VOL method for superconducting cavities.


[1] R. Garoby, A. Vergara, H. Danared *et al.*, The European Spallation source design, Phys. Scr. **93**, 014001 (2018).

[2] R. Miyamoto, C. Amstutz, S. Armanet *et al.*, Beam commissioning of normal conducting part and status of ESS project, in *Proceedings of the 31st Linear Accelerator Conference, Liverpool, UK* (JACoW, Geneva, Switzerland, 2022), 10.18429/JACoW-LINAC2022-MO1PA02.

[3] Y. Levinsen, R. Miyamoto, N. Milas *et al.*, ESS normal conducting LINAC commissioning results, in *Proceedings of the 68th ICFA Advanced Beam Dynamics Workshop on High-Intensity and High-Brightness Hadron Beams. HB2023, Geneva, Switzerland* (JACoW, Geneva, Switzerland, 2023),10.18429/JACoW-HB2023-TUA3I3

[4] Y. Levinsen, M. Akhyani, R. Baron *et al.*, (First RF phase scans at the European Spallation Source, in *Proceedings of the 11th International Beam Instrumentation Conference, Kraków, Poland* (JACoW, Geneva, Switzerland, 2022), 10.18429/JACoW-IBIC2022-TUP35.

[5] A. Feschenko, S. Bragin, Y. Kiselev *et al.*, Development and implementation of procedure for the SNS LINAC, in *Proceedings of the 21st Particle Accelerator Conference, Knoxville, TN, 2005* (IEEE, Piscataway, NJ, 2005), pp. 3064–3066.10.1109/PAC.2005.1591365

[6] K. Crandall, The AT tune-up procedure for the LAMPF. 805-MHz linac, Los Alamos Laboratory, Report No. LA-6374-MS, 1976. Available at https://www.osti.gov/servlets/purl/7353211.

[7] R. Zeng and O. Troeng, Transient beam loading based calibration for cavity phase and amplitude setting, in *Proceedings of the 57th ICFA Advanced Beam Dynamics Workshop on High-Intensity and High-Brightness Hadron Beams, Malmö, Sweden* (JACoW, Geneva, Switzerland, 2016). Available athttps://accelconf.web.cern.ch/hb2016/papers/mopl025.pdf.

[8] J. Galambos, A. Aleksandrov, C. Deibele *et al.*, Pasta—an RF phase scan and tuning application, in *Proceedings of the 21st Particle Accelerator Conference, Knoxville, TN, 2005* (IEEE, Piscataway, NJ, 2005), pp. 1491–1493, 10.1109/PAC.2005.1590810.

[9] Y. Zhang, I. Campisi, P. Chu *et al.*, Determination of field amplitude and synchronous phase using the beam-induced signal in an unpowered superconducting cavity, Nucl. Instrum. Methods Phys. Res., Sect. A **571**, 574 (2007).

[10] S. N. Simrock and T. Schilcher, DESY, Transient beam loading based calibration of the vector-sum for the TESLA test facility, in *Proceedings of the 8th Workshop on RF Superconductivity, Abano Terme, Italy* (1997), pp. 786–790, https://accelconf.web.cern.ch/e96/PAPERS/THPL/THP025L.PDF.

[11] P. Pawlik, M. Grecki, S. Simrock, and A. Napieralski, New method for beam induced transient measurement, Meas. Sci. Technol. **18**, 2348 (2007). https://doi.org/10.1088/0957-0233/18/8/008

[12] N. Walker, Experience with beam-transient LLRF calibration in XFEL, in *Proceedings of the Oral Presentation of DESY-TEMF Collaboration Meeting* (2020). Available at https://www.temf.tu-darmstadt.de/media/temf_emft/pdfs/desy/2020-11-02_Nick_Walker_Calibration.pdf.

[13] N. Walker, V. Ayvazyan, J. Branlard *et al.*, Beam-transient-based LLRF voltage signal calibration for the European XFEL, in JACoW, 2022), *Proceedings of 31st Linear Accelerator Conference, LINAC-2022, Liverpool, UK* (Geneva, Switzerland,10.18429/JACoW-LINAC2022-MOPOPA03.

[14] C. Xu, Z. Zhu, F. Qiu *et al.*, Application of a modified iterative learning control algorithm for superconducting radio-frequency cavities, Nucl. Instrum. Methods Phys. Res., Sect. A **1026**, 166237 (2022)..

[15] R. Zeng, Approach to calibrate beam phase using steady-state RF forward signal under closed-loop operation, in *Proceedings of the 11th Low-Level Radio Frequency Workshop, Gyeongju, Republic of Korea* (2023), https://www.indico.kr/event/29/contributions/374/.

[16] F. Qiu, On-line beam synchronous phase calibration using beam-induced rf signals, in *Proceedings of the Invited oral presentation of the 13th International Beam Instrumenta-*

*tion Conference, Beijing, China* (2024), https://indico.jacow.org/event/80/contributions/5837/.

[17] L. J. Yang, On-line beam phase and current measurement using deep learning models, *Proceedings of the Oral Presentation of the 2024 LLRF Topical Workshop—timing, synchronization, Measurements and Calibration, LLRF-2024, Rome, Italy* (2024). Available at https://agenda.infn.it/event/42239/contributions/244839/..

[18] M. Grecki, V. Ayvazyan, J. Branlard *et al.*, On-line RF amplitude and phase calibration, in *Proceedings of the 8th International Particle Accelerator Conference, IPAC-2017, Copenhagen, Denmark* (JACoW, Geneva, Switzerland, 2017), pp. 3957–3960 10.18429/JACoW-IPAC2017-THPAB103

[19] F. Qiu, C. Y. Xu, R. H. Zeng *et al.*, Online beam phase calibration with detuning compensation for normal-conducting cavities under closed-loop operation, Nucl. Sci. Tech. **37**, 108 (2026).

[20] F. Qiu, J. Y. Ma, G. D. Jiang *et al.*, Approach to calibrate actual cavity forward and reflected signals for continuous wave-operated cavities, Nucl. Instrum. Methods Phys. Res., Sect. A **1034**, 166769 (2022).10.1016/j.nima.2022.166769.

[21] F. Qiu, J. Y. Peng, S. H. Wei *et al.*, Analytical modeling and experimental verification of oscillatory ponderomotive instabilities in closed-loop superconducting rf cavities, Phys. Rev. Accel. Beams **28**, 112001 (2025).

[22] T. Schilcher. Vector sum control of pulsed accelerating fields in Lorentz force detuned superconducting cavities, Ph.D. thesis, University of Hamburg, 1998,https://bib-pubdb1.desy.de/record/291638/files/.

[23] A. Brandt. Development of a finite state machine for the automated operation of the LLRF control at FLASH Ph.D. thesis, University of Hamburg, 2007, https://www.osti.gov/etdeweb/biblio/20930559.

[24] F. Qiu, S. Michizono, T. Miura *et al.*, Real-time cavity simulator-based low-level radio-frequency test bench and applications for accelerators, Phys. Rev. Accel. Beams **21**, 032003 (2018).

[25] R. Huang and Y. He, A phenomenological model of the fundamental power coupler for a superconducting resonator, Nucl. Sci. Tech. **34**, 67 (2023).

[26] F. Qiu, Y. He, A.-D. Wu *et al.*, In situ mitigation strategies for field emission-induced cavity faults using low-level radiofrequency system, Nucl. Sci. Tech. **33**, 140 (2022).

[27] J. Y. Ma, L. J. Yang, F. Qiu *et al.*, Virtual cavity probe for the real-time identification of cavity burst-noise type in superconducting radio-frequency systems, Nucl. Instrum. Methods Phys. Res., Sect. A **1068**, 169786 (2024).

[28] J. Y. Ma, C. Y. Xu, A. D. Wu *et al.*, Measurement of the cavity-loaded quality factor in superconducting radio-frequency systems with mismatched source impedance, Nucl. Sci. Tech. **34**, 123 (2023).

[29] J. Y. Ma, L. J. Yang, F. Qiu *et al.*, Application of a new cavity-loaded factor calibration algorithm on the Test Stand 2 facility at the European Spallation Source, Radiat. Detect. Technol. Methods **8**, 1520 (2024).

[30] R. Zeng, W. Schappert, and P. Jönsson, Application investigation of high precision measurement for basic cavity parameters at ESS, in *Proceedings of the 27th Linear Accelerator Conference, LINAC-2014, Geneva, Switzerland* (JACoW, Geneva, Switzerland, 2014), pp 115–117, 10.18429/JACoW-LINAC2014-MOPP040

[31] O. González, N. Garmendia, P. González *et al.*, RF design and low power measurements of a nose cone single gap buncher cavity, in *Proceedings of the 27th Linear Accelerator Conference, LINAC-2014, Geneva, Switzerland* (JACoW, Geneva, Switzerland, 2014), pp. 1003–1005.10.18429/JACoW-LINAC2014-THPP025

[32] Y. Zhang, I. Campisi, P. Chu *et al.*, Comparison of SNS superconducting cavity calibration methods, in *Proceedings of the 23rd International Linac Conference, LINAC-2006, Knoxville, TN, 2006* (JACoW, Knoxville, TN, 2006), pp. 436–438, 10.18429/JACoW-LINAC2006-TUP032.

[33] L. Gong, R. Zeng, C. Xu *et al.*, On-line measurement of beam phase and energy gain based on beam-cavity interaction, Phys. Rev. Accel. Beams **28**, 122801 (2025).

[34] J. C. Yang, J. W. Xia, G. Q. Xiao *et al.*, High intensity heavy ion accelerator facility (HIAF) in China, Nucl. Instrum. Methods Phys. Res., Sect. B **317**, 263 (2013). https://doi.org/10.1016/j.nimb.2013.08.046.

[35] X. Zhou, J. Yang, and H. I. A. F. project team, Status of the high-intensity heavy-ion accelerator facility in China, AAPPS Bull. **32**, 35 (2022)..

[36] J. C. Yang and H. I. A. F. project team, Status of the HIAF Accelerator Facility in China, in *Proceedings of the 16th International Conference on Heavy Ion Accelerator Technology, HIAT2025, East Lansing, MI* (JACoW, Geneva, Switzerland, 2025),10.18429/JACoW-HIAT2025-MOY01.

[37] M. Xu, Y. He, S. Zhang *et al.*, Low beta superconducting cavity system design for HIAF iLinac, Nucl. Eng. Technol. **55**, 2466 (2023).